Cell Reports

Article

Cilium induction triggers differentiation of glioma stem cells

Graphical abstract

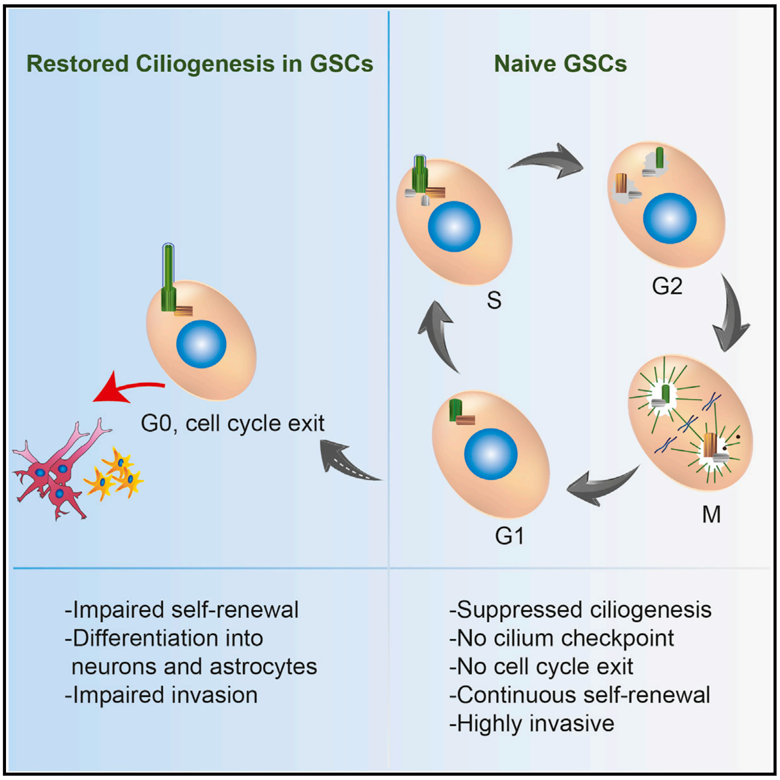

Highlights

- Cilium checkpoint regulates self-renewal and differentiation of neural stem cells
- GSCs have suppressed ciliogenesis and thus have no cilium checkpoint
- Reintroducing of cilia in GSCs switches them from self-renewal to differentiation state
- GSCs reintroduced with cilia do not invade brain organoids

Authors

Gladiola Goranci-Buzhala,
Aruljothi Mariappan,
Lucia Ricci-Vitiani, ..., Argyris Papantonis,
Roberto Pallini, Jay Gopalakrishnan

Correspondence

jay.gopalakrishnan@hhu.de

In brief

A precise temporal cilium disassembly is critical for regulating self-renewal and differentiation of NPCs. Goranci-Buzhala et al. report that patient-derived glioma stem cells are similar to NPCs but have suppressed ciliogenesis that promotes self-renewal and blocks differentiation. Reintroducing cilia switches them from self-renewal to differentiation, offering potential therapeutic strategies for glioma.

Goranci-Buzhala et al., 2021, Cell Reports *36*, 109656
September 7, 2021 © 2021 The Author(s).
https://doi.org/10.1016/j.celrep.2021.109656

CellPress

Cell Reports

CellPress
OPEN ACCESS

Article

Cilium induction triggers differentiation of glioma stem cells

Gladiola Goranci-Buzhala,[1,10] Aruljothi Mariappan,[1,10] Lucia Ricci-Vitiani,[2] Natasa Josipovic,[3] Simone Pacioni,[4] Marco Gottardo,[1] Johannes Ptok,[5] Heiner Schaal,[5] Giuliano Callaini,[6] Krishnaraj Rajalingam,[7] Brian Dynlacht,[8] Kamyar Hadian,[9] Argyris Papantonis,[3] Roberto Pallini,[4] and Jay Gopalakrishnan[1,11,*]

[1]Institute of Human Genetics, University Hospital Düsseldorf, Heinrich-Heine-Universität, Universitätsstr. 1, 40225 Düsseldorf, Germany
[2]Department of Oncology and Molecular Medicine, Istituto Superiore di Sanità, Rome 00161, Italy
[3]Institute of Pathology, University Medicine Göttingen, Georg-August University Göttingen, Robert-Koch-Straße 40, 37075 Göttingen, and Center for Molecular Medicine, University of Cologne, 50931 Cologne, Germany
[4]Institute of Neurosurgery, Fondazione Policlinico Universitario A. Gemelli IRCCS-Università Cattolica del Sacro Cuore, Rome 00168, Italy
[5]Institute of Virology, Medical Faculty, University Hospital Düsseldorf, Heinrich-Heine-Universität, Universitätsstr. 1, 40225 Düsseldorf, Germany
[6]Department of Life Sciences University of Siena, Via Aldo Moro 2, Siena 53100, Italy
[7]Cell Biology Unit, University Medical Center, Johannes Gutenberg University Mainz, Langenbeckstr. 1, 55131 Mainz, Germany
[8]Department of Pathology and NYU Cancer Institute, NYU School of Medicine, New York, NY 10016, USA
[9]Assay Development and Screening Platform, Institute of Molecular Toxicology and Pharmacology, Helmholtz Zentrum München, Ingolstädter Landstr.1, 85764 Neuherberg, Germany
[10]These authors contributed equally
[11]Lead contact
*Correspondence: jay.gopalakrishnan@hhu.de

https://doi.org/10.1016/j.celrep.2021.109656

SUMMARY

Glioblastoma multiforme (GBM) possesses glioma stem cells (GSCs) that promote self-renewal, tumor propagation, and relapse. Understanding the mechanisms of GSCs self-renewal can offer targeted therapeutic interventions. However, insufficient knowledge of GSCs' fundamental biology is a significant bottleneck hindering these efforts. Here, we show that patient-derived GSCs recruit elevated levels of proteins that ensure the temporal cilium disassembly, leading to suppressed ciliogenesis. Depleting the cilia disassembly complex components is sufficient to induce ciliogenesis in a subset of GSCs via relocating platelet-derived growth factor receptor-alpha (PDGFR-α) to a newly induced cilium. Importantly, restoring ciliogenesis enabled GSCs to switch from self-renewal to differentiation. Finally, using an organoid-based glioma invasion assay and brain xenografts in mice, we establish that ciliogenesis-induced differentiation can prevent the infiltration of GSCs into the brain. Our findings illustrate a role for cilium as a molecular switch in determining GSCs' fate and suggest cilium induction as an attractive strategy to intervene in GSCs proliferation.

INTRODUCTION

Glioblastoma (GBM) is the most frequent malignant primary brain tumor (Matsukado et al., 1961; Ostrom et al., 2014; Ferreri et al., 2010). Despite surgical resection, its rapid growth, resistance to chemotherapy, and high invasiveness cause GBM patients succumb to the disease with a median survival time of 15 months (Stupp et al., 2005; Johnson and O'Neill, 2012). Low passage patient-derived glioma stem cells (GSCs) are phenotypically similar to *in vivo* tumors characterized by their self-renewal and multi-lineage differentiation (Singh et al., 2003; Jacob et al., 2020; Pine et al., 2020, Wang et al., 2019; Lathia et al., 2015). These cell types are responsible for most aspects of tumor initiation, maintenance, and invasion *in vivo*, and thus, GSCs are the accepted models of GBM biology (Suvà et al., 2014; Liau et al., 2017). GSCs possess neural stem cell attributes exhibiting uncontrolled self-renewal properties. This could be due to genetic alterations in GSCs, adaptation between proliferative and slow-cycling states, and enrichment of stemness on therapy (Liau et al., 2017; Park et al., 2017; Ricci-Vitiani et al., 2010; Rajakulendran et al., 2019; Neftel et al., 2019; Wang et al., 2019). However, it remains unclear whether there are also alterations in cellular structures implicated in cell cycle control, self-renewal, and differentiation of GSCs. Intense efforts are being made to understand the mechanisms of GSCs proliferation that can be exploited for therapeutic interventions.

The primary cilium is a microtubule-based cellular structure in which the minus end of the ciliary microtubule is anchored to a basal body that serves as a template for the assembly of the ciliary microtubule (Figure S1A) (Anvarian et al., 2019; Larsen et al., 2013). The cilium serves as a "cellular antenna" sensing multiple signals, including sonic hedgehog (Shh), G-protein coupled receptors, and receptor tyrosine kinase (Schmidt et al., 2002; Schou et al., 2015; Nachury and Mick, 2019). In

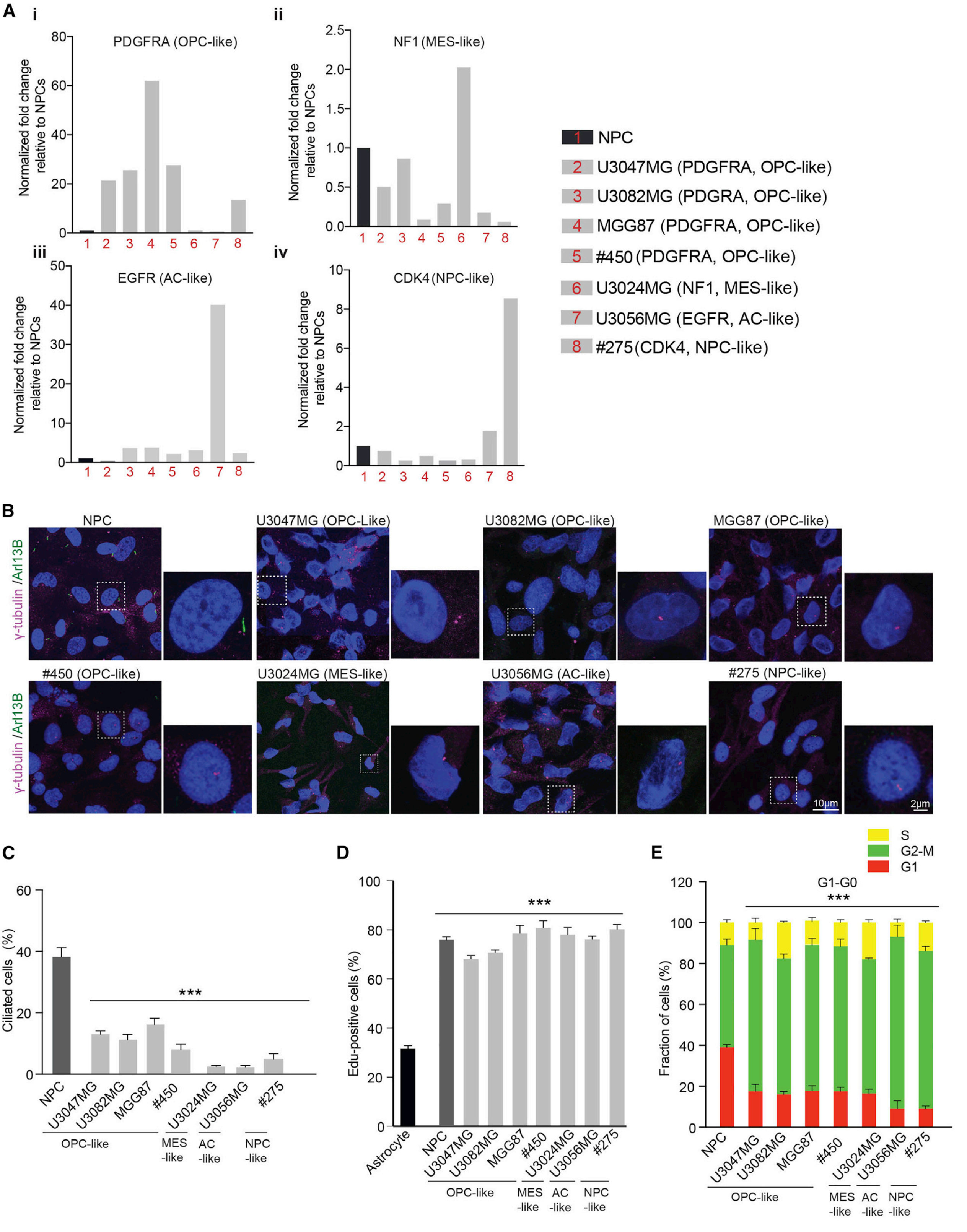

(legend on next page)

cycling cells, the cilium assembly occurs during cell cycle exit (G1-G0), and disassembly coincides with cell cycle re-entry (G1-S to M) (Jackson, 2011). A delay or failure in cilium disassembly could act as a brake, retaining cells in G0/G1 and transiently preventing cell cycle progression. This provides a conceptually novel "cilium checkpoint" regulating cell cycle progression (Figure S1B). Studies have recently begun to uncover the mechanisms linking cilia disassembly to cell cycle re-entry and identified mitotic kinases such as Aurora-A, Plk1, and Nek2 that can trigger cilium disassembly (Kim et al., 2011; Wang et al., 2013; Pugacheva et al., 2007). However, whether these protein components are assembled as a cytoplasmic complex, presumably as a cilia disassembly complex (CDC), has remained unknown for a precise temporal cilia disassembly.

CPAP, a conserved centrosomal protein, provides a scaffold for recruiting CDC components of Nde1, HDAC6, Aurora-A, and OFD1, to the ciliary base that is critical for temporal cilia disassembly at the onset of cell cycle re-entry (Gabriel et al., 2016). The precise timing of cilia disassembly ensures the length of G1-S transition and, thus, the self-renewal property of NPCs (Gabriel et al., 2016; Kim et al., 2011; Li et al., 2011). Prolonging the G1 phase due to a delayed cilia disassembly is sufficient to cause premature differentiation of NPCs into early neurons, leading to an overall reduction in the NPCs pool (Gabriel et al., 2016). In summary, these studies have successfully modeled the critical function of cilia dynamics in NPC maintenance.

Interestingly, frequent loss of cilia is common in various types of cancers, including breast, prostate, skin, melanoma, and pancreatic tumors (Seeley and Nachury, 2009; Fabbri et al., 2019; Zingg et al., 2018). So far, only a few reports have characterized loss of cilium in cultured GBM cells raising the question of whether cilia loss is due to cell culture artifacts, suppressed ciliogenesis, or perturbation of normal cilium formation (Yang et al., 2013; Moser et al., 2009). Although the loss of cilia in GBM has been reported, only Moser et al. (2014) have conducted an ultrastructural study using GBM tumors. Their study characterized that disruptions occur at the early stages of ciliogenesis, questioning the identity of candidate proteins that suppress the early stages of ciliogenesis (Moser et al., 2009). From this, we speculated that patient-derived GSCs have suppressed ciliogenesis at the early stage of ciliogenesis, and CDC proteins are involved in this critical period to suppress ciliogenesis. This may provide a selective advantage to GSCs to continuously self-renew without cell cycle exit and differentiation (Figure S1B, right panel). If so, we hypothesize that perturbing these CDC components could promote ciliogenesis, and as a result, this may impair the self-renewal of GSCs and trigger them to differentiate (Figure S1C).

In this work, we show that irrespective of various cellular states of GBM, a panel of tested patient-derived GSCs and clinical glioma tissues exhibit suppressed ciliogenesis due to elevated levels of CDC recruitment to basal bodies. We then established that preventing CDC recruitment and altering their dynamic localization behavior at the basal body is sufficient to induce cilium in a subset of GSCs that overexpress constitutively active receptor tyrosine kinase platelet-derived growth factor receptor-alpha (PDGFR-α). Upon cilium induction, PDGFR-α is sequestered to newly induced cilium from its original location with concomitant reduction of overall PDGFR-α levels. Inducing ciliogenesis triggers GSCs switching from self-renewal to differentiation state. Finally, we demonstrate that GSCs induced with cilia failed to infiltrate into induced pluripotent stem cell (iPSC)-derived human brain organoids and mouse brain, suggesting that cilium induction can play an instructive role in determining GSCs' fate.

RESULTS

Patient-derived GSCs exhibit suppressed ciliogenesis

To test if low-passage GSCs display suppressed ciliogenesis, we investigated at least seven patient-derived GSC lines and nine clinical glioblastoma tissues. First, we aimed to categorize the cellular states of GSC lines. A recent report indicated that GBM cells exist within four cellular states of neural-progenitor-like (NPC-like), oligodendrocyte-progenitor-like (OPC-like), astrocyte-like (AC-like), and mesenchymal-like (MES-like). Interestingly, each cellular state associates with a distinct signature of genetic alterations occurring in CDK4 (NPCs-like), PDGFRA (OPC-like), EGFR (AC-like), and NF1 (MES-like) (Neftel et al., 2019). To analyze the coexistence of these cellular states in our primary GSC cultures, we quantified relative gene expressions of CDK4, PDGFRA, EGFR, and NF1. These genes' relative expression levels serve as representatives of each cellular state and hint at various cellular states. Therefore, we measured their levels to categorize our GSCs cultures as NPCs-like, OPC-like, AC-like, and MES-like states.

We noticed that although each of these states coexists in an individual GSC line, one state is predominantly existing over the other three in any GSC line we tested (Figure 1A). Thus, by

Figure 1. Patient-derived GSCs exhibit suppressed ciliogenesis

(A) qRT-PCR analysis of *PDGFRA* (i), *NF1* (ii), *EGFR* (iii), and *CDK4* (iv) relative to NPCs reveal various cellular states. The calculated values were normalized to *GAPDH* expression, and the values given are relative to healthy NPCs. The values are mean from three technical replicates from n = 2 independent experiments.

(B) Compared to iPSCs-derived NPCs, GSCs of different cellular statuses exhibit suppressed ciliogenesis. Arl13B (green) labels cilia and γ-tubulin (magenta) labels centrosomes. Scale bar, 10 μm (overview), 2 μm (inset). At least 500 cells for each cell line from n = 4 independent experiments were tested.

(C) The bar diagram quantifies frequencies of ciliated cells. Note that compared to NPCs, GSCs of different cellular statuses displays an overall decrease in ciliation. At least 500 cells in each cell line from n = 3 independent experiments were tested. One-way ANOVA followed by Dunnett's multiple comparisons test ***$p < 0.001$. Error bars show mean ±SEM.

(D) The bar diagram quantifies frequencies of EdU-positive cells. Note that GSCs exhibit a similar EdU profile of NPCs and exhibit an increased EdU incorporation compared to ciliated cycling astrocytes. At least 300 cells in each cell line from n = 3 independent experiments were tested. One-way ANOVA, followed by Dunnett's multiple comparisons test, ***$p < 0.001$. Error bars show mean ± SEM.

(E) The bar diagram quantifies cell cycle analysis by fluorescence ubiquitin cell cycle indicator (FUCCI) tracing. Note that a significant fraction of GSCs and NPCs are retained at G2-M (green). At least 100 cells in each cell line from n = 4 independent experiments were tested. Ordinary two-way ANOVA, followed by Tukey's multiple comparisons test, ***$p < 0.001$. Error bars show mean ± SEM.

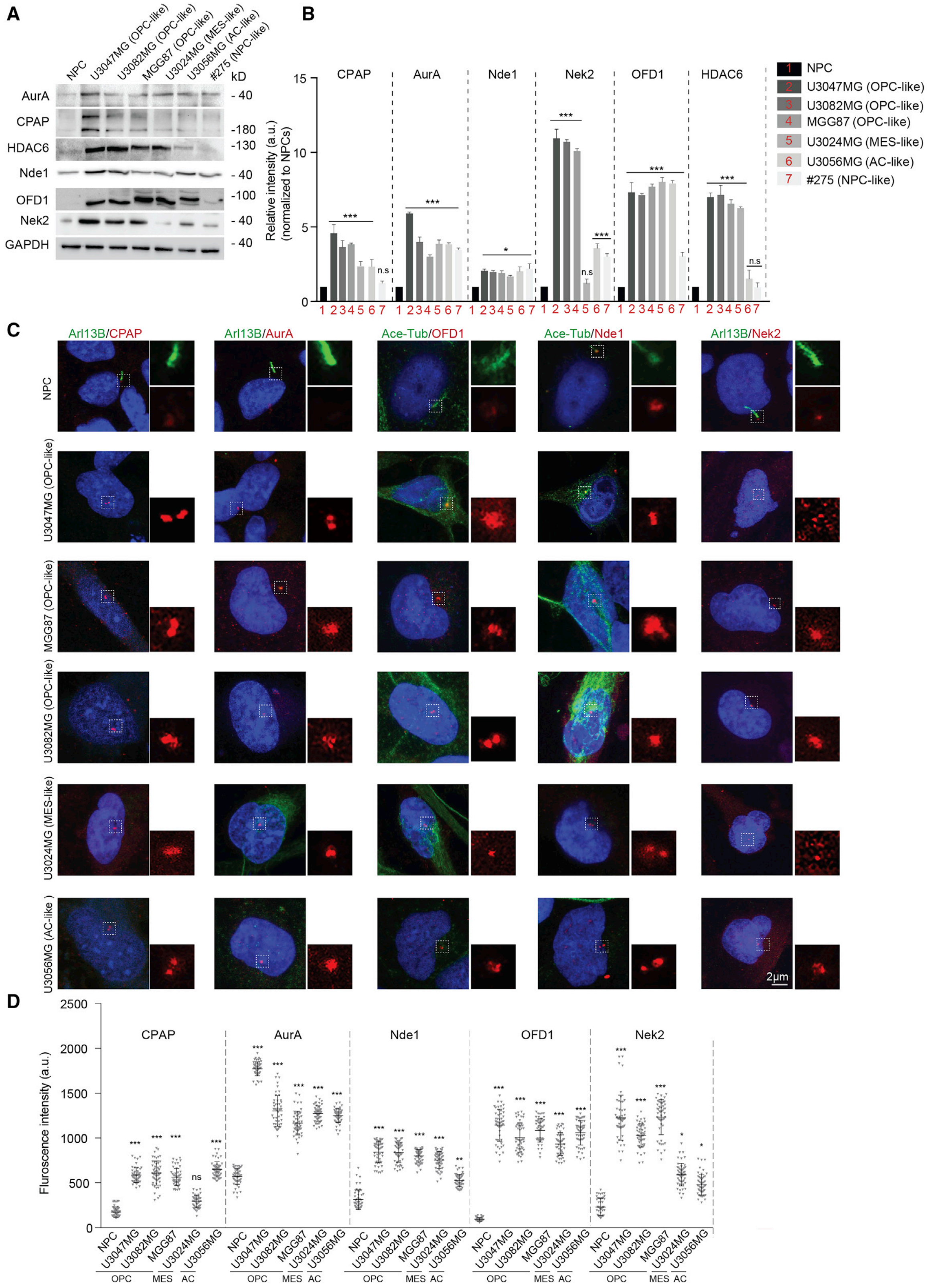

(legend on next page)

measuring these gene's relative expression levels, we categorized our patient-derived GSCs according to the known cellular states of GBM (Figure 1A). We then determined that GSCs display neural stem cell markers similar to iPSCs-derived neural progenitor cells (NPCs) (Figure S2A). Scoring cilia, we noticed that only a fraction of GSCs displayed cilia suggesting that suppressed ciliogenesis is a common denominator irrespective of the cellular status. Like cultured GSCs, WHO grade IV GBM tissues also revealed reduced frequencies of ciliated cells (Figures 1B, 1C, S2B, and S2C).

Delayed cilia disassembly is associated with suppression of cell division via an extended G1-S transition while an accelerated cilia disassembly or loss of cilia promoted cell proliferation (Gabriel et al., 2016; Kim et al., 2011; Li et al., 2011; Pugacheva et al., 2007). Because ciliogenesis is suppressed in all tested GSCs, we speculated that these GSCs would exhibit an increased proliferation. Our 24-h pulse labeling using ethynyldeoxyuridine (EdU) revealed that in contrast to proliferating ciliated astrocytes, an increased number of GSCs with EdU incorporation was observed (Figure 1D). Furthermore, our fluorescence ubiquitination cell cycle indicator (FUCCI)-based analyses revealed that similar to fast proliferating NPCs, only a small fraction of GSCs reside at G1/G0, a cell cycle stage at which the cilium assembly occurs in healthy cells (Figure 1E). These data suggest that suppressed ciliogenesis in GSCs is associated with increased proliferation.

GSCs have an elevated level of CDC components

Because cilia formation is suppressed in GSCs at the early stages of ciliogenesis, we speculated that CDC protein levels are elevated in this critical period to suppress ciliogenesis, allowing cells to proliferate continuously. Studies have shown that Nek2, an S/G2 kinase, is elevated in cancer cells and plays a prominent role in cilia disassembly by activating its physiological substrate Kif24, a depolymerizing microtubule kinesin that suppresses cilia formation (Kim et al., 2015). By analyzing purified FLAG-tagged CPAP complexes from HEK cell extracts, we first identified that Nek2 co-purifies with the known components of the CDC that are conserved components across several cell types (Pugacheva et al., 2007; Gabriel et al., 2016; Kim et al., 2015; Kobayashi et al., 2011; Inaba et al., 2016; Tang et al., 2013). Reciprocally, CDC components of Aurora-A, HDAC6, Nde-1, OFD1, and CPAP co-purify with FLAG-tagged Nek2 complexes, which included Kif24 (Figure S3A). To test our speculation that GSCs exhibit an overall increase in CDC protein levels, we performed a semiquantitative western blot analysis by probing an equivalent quantity of protein extracts. GSCs extracts showed an overall increase in CDC components compared to ciliated NPCs (Figures 2A and B). Interestingly, we measured the highest rise of Nek2 in OPC-like GSCs. Finally, immunostaining of GSC lines using specific antibodies further revealed that compared to NPCs, basal bodies of GSCs that exhibit suppressed ciliogenesis recruit an enhanced level of these proteins (Figures 2C and 2D).

To assess if CDC upregulation could be corroborated in GBMs and obtain insight into the mechanisms by which CDC components are upregulated in GSCs, we analyzed the publicly available transcriptomic datasets. First, we examined the GlioVis portal that displays publicly available TCGA-GBM RNA sequencing (RNA-seq) datasets of 538 disease and 10 non-tumor samples. Compared to non-tumor samples, we observed a significant fold change in mRNA expression levels of essential CDC genes such as *NEK2* and *CPAP*, indicating CDC components are upregulated in GBM (Figure S3B). Second, we analyzed both RNA transcriptomic and microarray data derived from cells harboring H3K27 trimethylation (H3K27me3) (Chan et al., 2013; Haag et al., 2021). Approximately 60% of high-grade pediatric glioma has a Lys 27-to-methionine (K27M) mutation in histone H3 variant H3.3 H3K27me3, and Ezh2 (the catalytic subunit of H3K27 methyltransferase) at chromatin are increased at hundreds of gene loci in these patient samples. This gain of H3K27me3 and Ezh2 at gene promoters has altered gene expression associated with various cancer pathways. Analyzing the RNA-seq of patient cells (SF7761 and SF8828) and control neural stem cell (NSC) cell lines, we noticed that CDC genes are upregulated in patient cells (Figure S3C). Similarly, some of these CDC genes were also upregulated in microarray data that used K27M-overexpressing NSCs (Figure S3D) (Haag et al., 2021). Together, these data indicate that CDC components are possible candidate proteins whose elevated levels could suppress ciliogenesis in tested GSCs.

Suppressing CDC level induces cilia in GSCs

We developed a proof-of-principle assay by testing if depletion of CDC components can induce cilia in U3047MG cultures. First, we established short hairpin RNA (shRNA)-mediated depletion of selected CDC components. We then scored the frequencies of ciliated cells in cultures that were depleted with individual CDC components. This analysis has narrowed down Nek2 because we detected the highest increase of ciliated cells in Nek2 depleted cultures (Figure S4A).

Therefore, we chose to use Nek2 as a tool in our experiments for a few reasons. First, due to its relatively smaller size, we were able to handle the construct in multiple experiments. Second, Nek2, but not catalytically inactive Nek2 (Nek2-KD, Nek2-kinase-dead where lysine is replaced with arginine, Nek2-K37R),

Figure 2. GSCs have elevated levels of CDC components

(A) Semiquantitative western blot exhibiting relative levels of tested CDC components between healthy NPCs and GSCs of different cellular statuses. An equivalent quantity of cell extracts was loaded. GSCs show an overall elevated level of CDC components. GAPDH was used as a loading control.

(B) The bar diagram quantifies the relative intensity of tested CDC components in healthy NPCs and GSCs. Western blots from n = 3 independent experiments. Ordinary two-way ANOVA followed by Sidak's multiple comparisons test, ***$p < 0.001$, *$p < 0.05$. ns, non-significant. Error bars show mean ± SEM.

(C) Compared to NPCs, GSCs of different cellular statuses recruit an enhanced level of CDC components at the ciliary base. Cilia are labeled either by Arl13B or acetylated α-tubulin (green). CDC components (red) were immunostained using antibodies specific to CPAP, Aurora-A, OFD1, Nde1, and Nek2. Scale bar, 2 μm.

(D). Bar diagram quantifies fluorescence signal intensity. At least 200 cells in each cell line from n = 4 independent experiments were tested. Ordinary one-way ANOVA followed by Tukey's multiple comparisons test. ***$p < 0.001$, **$p < 0.01$, *$p < 0.05$. ns, non-significant. Error bars show mean ± SEM.

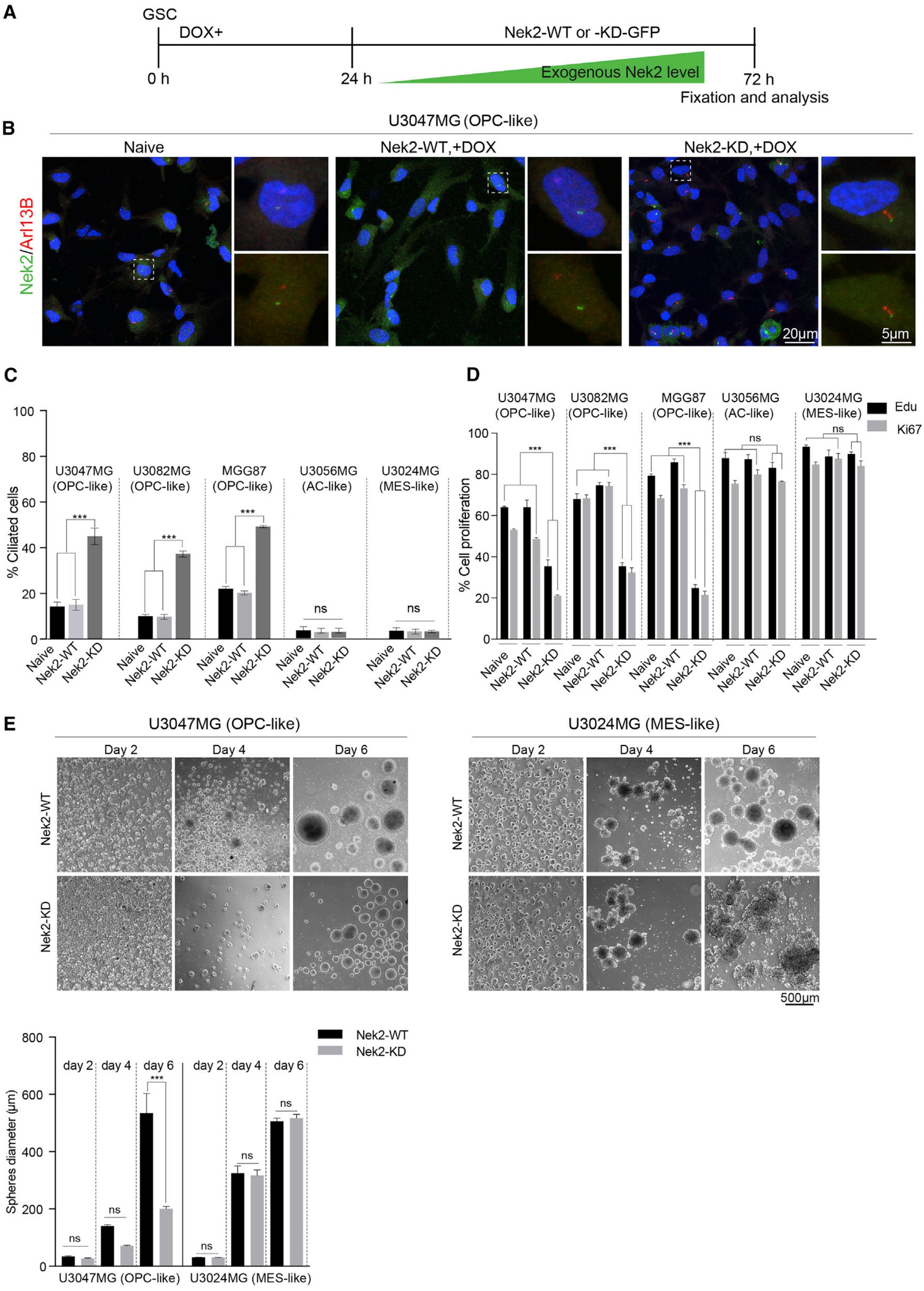

(legend on next page)

can phosphorylate its physiological substrate Kif24, a kinesin that depolymerizes ciliary microtubule (Kim et al., 2015; Fry et al., 1995; Kobayashi et al., 2011). Therefore, instead of depleting the endogenous Nek2 in our experiments, we could express both catalytically active and inactive versions in a controlled manner. To test if catalytically inactive Nek2 (Nek2-KD) is sufficient to induce cilia in GSCs, we generated GSC lines that were engineered to express green fluorescence protein (GFP)-tagged Nek2-WT and catalytically inactive Nek2-KD on doxycycline induction. The presence of GFP recognized the expressions of these inducible Nek2 variants.

In contrast to naive or Nek2-WT-expressing U3047MG GSCs, a significant number of Nek2-KD-expressing GSCs displayed cilia within 24 h after doxycycline-induction (Figures 3A and 3B). The frequencies of ciliated GSCs did not vary significantly after 72 h of doxycycline-induction (data not shown). Interestingly, Nek2-KD expression could induce cilia only in OPC-like GSC lines that exhibit the highest level of Nek2 expression (responder lines such as U3047MG, U3082MG, and MGG87) but not in other subsets of GSC lines (non-responder lines such as MES-, AC-, and NPC-like GSCs) (Figures 3C and S4B). Cell proliferation analysis determined by EdU incorporation and Ki67 staining indicated that responder lines proliferated significantly slower than non-responder lines (Figure 3D).

The finding that responder lines exhibiting reduced proliferation on cilium induction prompted us to speculate that these GSCs presumably do not form spheres, a typical characteristic of GSCs (Singh et al., 2003, 2004). Our sphere formation assay indicated that U3047MG GSCs formed spheres and progressively grew up to 600 μm in size. In contrast, Nek2-KD-expressing GSCs failed to grow beyond 200 μm. Importantly, control experiments that used a non-responder line (U3024MG) that did not respond to cilium induction continue to grow regardless of Nek2-KD expression (Figure 3E). Because perturbation of CDC induces cilium only in OPC-like GSCs, our further in-depth characterizations have been focused on U3047MG, a representative OPC-like GSC line.

To understand the plausible mechanisms of cilium induction, we analyzed the CDC proteins' levels before and after cilium induction. Western blots of U3047MG cell extracts revealed an overall reduction in CDC protein levels after cilia induction (Figure S5A). We reasoned that this could be due to the general decrease in proliferation and retention of cells at G1-G0 as a normal process associated with cell cycle exit or transient quiescence (G0 or G1) (Pugacheva et al., 2007; Gabriel et al., 2016). This prompted us to estimate the individual CDC component's recruitment to the basal bodies. Immunostaining using specific antibodies revealed that CDC components' recruitment is drastically reduced after cilium induction (Figure S5B).

Newly induced cilia are persistent and structurally and functionally normal

Because cilium induction in responder lines impairs GSCs proliferation (Figure 3D), we conducted a FUCCI-based analysis on U3047MG cells. This analysis revealed that a significant fraction of U3047MG cells reside at G1/G0 after cilia induction (Figure S6A) and prompted us to speculate that Nek2-KD-induced cilia are persistent; thus, cells presumably did not proceed to G2-M transition. To test this, we withdrew doxycycline from both responder (U3047MG) and non-responder (U3024MG) GSC lines after day 3 and continued culturing for a prolonged period of up to 10 days. Although Nek2 expression is unnoticeable at day 10, the abundance of ciliated cells in U3047MG cultures remains unchanged. Concurrently, cell proliferation did not continue. In contrast, the non-responder control U3024MG that could not be induced with cilia continued to proliferate. These findings indicate that newly induced cilia are persistent and suggest that once ciliated, these GSCs do not re-enter the cell cycle (Figure 4A).

Turning our analysis at the ultrastructural level, we analyzed centrioles of U3047MG at an early stage of ciliogenesis where centriole assembles ciliary vesicle and anchors at the membrane serving as a basal body (Moser et al., 2014). Compared to NPCs, centrioles of U3047MG contained swollen and misshaped ciliary vesicles revealing a suppressed ciliogenesis at the early stages of cilium formation. We also noticed the frequent presence of electron-dense satellite-like particles concentrated at the vicinities of basal bodies, which may be corroborated with an elevated level of CDC components in un-ciliated naive GSCs (Figure S6B, i and ii). On the other hand, we noticed that newly induced cilia structurally appear normal with an infrequent presence of electron-dense particles (Figure S6B, iii).

To analyze the functionality of newly induced cilia, we first tested for the presence of intraflagellar protein-88 (IFT88) and identified that the newly induced cilia were immunoreactive to IFT88 antibodies (Figure 4B). Next, we tested whether newly

Figure 3. Catalytically inactive Nek2 kinase induces primary cilia in GSCs

(A) Experimental scheme. Seeded GSCs were induced to express GFP-tagged Nek2-WT and Nek2-KD (kinase-dead, catalytically inactive), fixed, and analyzed.

(B) Compared to naive or Nek2-WT-expressing U3047MG (OPC-like), Nek2-KD-expressing cells display cilia. Nek2 (green) labels centrosomes. Arl13b labels cilia (red). Scale bar, 20 μm (overview), 5 μm (inset). n = 4 independent experiments.

(C) The bar diagram quantifies frequencies of ciliated cells across different GSCs on Nek2-KD expression. Nek2-KD could induce ciliogenesis selectively in OPC-like (U3047MG, U3082MG, and MGG87) GSCs and not in MES-like (U3024MG) or AC-like (U3056MG) GSCs. At least 300 cells in each cell line from n = 5 independent experiments were tested. Ordinary two-way ANOVA followed by Tukey's multiple comparisons test. ***$p < 0.001$, ns ,non-significant. Error bars show mean ± SEM.

(D) Cilium induction impairs the proliferation of OPC-like (U3047MG, U3082MG, and MGG87) GSCs but not in MES-like (U3024MG) or AC-like (U3056MG) GSCs. Bar diagram quantifies cell proliferation profile of naive, Nek2-WT-, and Nek2-KD-expressing GSC lines revealed by 48 h EdU pulse-chasing Ki67 immunoreactivity. At least 400 cells in each cell line from n = 4 independent experiments were tested. Ordinary two-way ANOVA followed by Sidak's multiple comparisons test. ***$p < 0.001$. ns, non-significant. Error bars show mean ± SEM.

(E) Cilium induction impairs neurosphere formation of OPC-like U3047MG but not MES-like U3024MG. Bar diagram quantifies sphere diameter of Nek2-WT- and Nek2-KD-expressing cells. At least 500 spheres in each cell line from n = 3 independent experiments were tested. Ordinary two-way ANOVA followed by Sidak's multiple comparisons test. ***$p < 0.001$. ns, non-significant. Error bars show mean ± SEM.

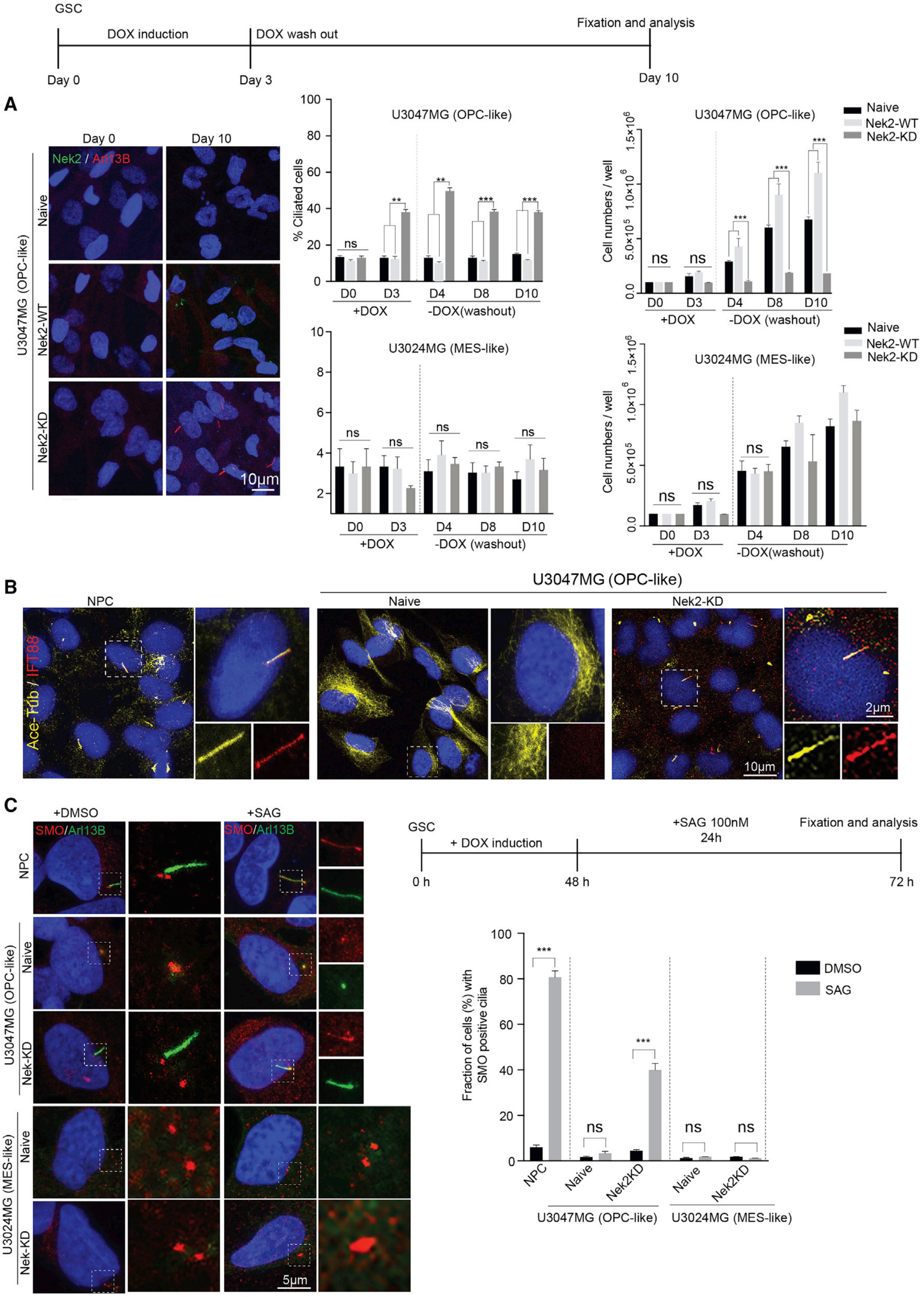

(legend on next page)

induced cilia can transduce sonic hedgehog (Shh) signaling because it acts through primary cilia (Goetz et al., 2009; Bangs and Anderson, 2017). Smoothened (Smo) is an integral part of the Shh pathway, which relocates to the cilium after activated by a smoothened agonist (SAG). On adding SAG, just like healthy NPCs, the activated Smo in U3047MG GSCs relocated from the basal body to the entire length of the cilium in GSCs (Figure 4C). These results collectively reveal that perturbing CDC recruitment is sufficient to induce structurally and functionally normal cilia in GSCs.

Cilium induction triggers GSCs differentiation

To dissect the consequences of cilium induction on GSCs, we tested whether they undergo differentiation. To our surprise, in contrast to unciliated naive GSCs, GSCs (responder lines of U3047MG, U3082MG, and MGG87) induced with cilia exhibited significantly increased proportions of GFAP, S100β, and TUJ1-positive cells, which are the identity markers of astrocytes and neurons. However, we could not detect any of these markers in the non-responder control U3024MG in which Nek2-KD expression did not induce cilia (Figures 5A and 5B). Importantly, responder GSC lines exhibited a strongly reduced immunoreactivity to Nestin, Pax-6, Sox2, and CD133, which specify neural and cancer stem cells (Figures 5A–5C). These findings indicate that cilium induction can determine GSCs' fate, and the differentiation process might be cilia dependent.

To further demonstrate that differentiation is a cilium-dependent process, we ablated cilia by depleting IFT88 (Loskutov et al., 2018). To this end, we first expressed Nek2-KD in U3047MG cells that were depleted of IFT88. As expected, we detected IFT88 immunoreactivity and the appearance of cilia in control small interfering RNA (siRNA)-treated cultures but not in IFT88 siRNA-treated cultures (Figure 6A). We then tested whether Nek2-KD could still induce differentiation of U3047MG cultures unable to assemble cilia due to IFT88 siRNA treatment. We first verified that IFT88 depletion did not induce GSCs differentiation. Importantly, Nek2-KD expression-induced differentiation of GSCs into GFAP and TUJ1-positive cells appears only in control siRNA-treated cultures but not in IFT88 siRNA-treated cultures (Figure 6B and the table summarize the findings). These data indicate that Nek2-KD-induced differentiation process is cilia-specific.

Cilium induction resets the aberrant PDGFR-α signaling in OPC-like GSCs

To dissect the mechanistic link between cilium induction and GSCs differentiation, we first investigated the global impact of cilia induction. We analyzed the transcriptome of U3047MG cells before and after cilium induction. We identified >1,500 differentially regulated genes (Figure S7A). Upregulated genes were associated with cell morphogenesis in differentiation, whereas downregulated genes were majorly associated with cell proliferation pathways (Figures S7B and S7C). Likewise, we noticed genes implicated in ciliogenesis were upregulated, whereas centrosome and CDC component genes involved in cell proliferation and cilia disassembly were downregulated (Figure S7D).

Interestingly, an unbiased analysis of the top 25 differentially expressed genes revealed that SOX10 and PDGFRA are strongly downregulated after cilium induction. Studies have demonstrated that PDGFRA is rapidly downregulated together with oligodendrocyte progenitor (OPC) lineage markers of SOX10 and OLIG2 when OPC differentiate into oligodendrocytes (Đặng et al., 2019; Rivers et al., 2008). Notably, downregulation of stemness maintenance and cell cycle regulators implicate cilium induction switches GSCs from self-renewal to differentiation state (Figures S7E and S7F). Together, the transcriptomic data corroborate with our microscopy-based analysis of cellular identities (Figure 5A).

We then analyzed the status of PDGFR-α signaling in U3047MG cells for several reasons. (1) There is a strong association between PDGFR-α overexpression, amplification, and mutation in OPC-like GBMs (Neftel et al., 2019) (Verhaak et al., 2010). (2) We detected an increased level of total PDGFR-α in OPC-like GSCs (Figure S7F) and indeed, PDGFR-α signaling is positively correlated to the self-renewal property of GSCs, accelerated tumor onset, and increased tumor invasion (Clarke and Dirks, 2003; Verhaak et al., 2010; Filbin et al., 2018; Brennan et al., 2013; Pathania et al., 2017). (3) PDGFR-α signaling is regulated by primary cilia in healthy cells (Schmid et al., 2018). (4) Cilium induction was significant in OPC-like GSCs (Figure 3C). Western blot analysis revealed that in contrast to un-ciliated U3047MG cells, ciliated cells showed a drastically reduced level of total PDGFR-α, which in turn correlated to reduced levels of its downstream signaling components such as activated pAKT and c-*myc*. This finding suggests that newly induced cilia in

Figure 4. Newly induced cilia in GSCs are persistent and normal in structure and function

(A) Experimental scheme of doxycycline induction and wash out. In the responder line (OPC-like U3047MG), Nek2-KD-expressing cells still harbor primary cilia at day 10 even after removing doxycycline (scale bar, 10 μm). Bar diagram at right quantifies the fraction of ciliated cells and absolute cell numbers at various time points of doxycycline wash out. Note that the non-responder line (MES-like U3024MG) in which cilium could not be induced continues to expand. At least 500 cells in each cell line from n = 3 independent experiments were tested. Ordinary two-way ANOVA followed by Tukey's multiple comparisons test. ***$p < 0.001$, **$p < 0.01$. ns, non-significant. Error bars show mean ± SEM.

(B) Just like healthy NPCs (left), newly induced cilia of U3047MG cells (right) display IFT88 particles (red). Cilia are labeled by acetylated α-tubulin (yellow). Naive U3047MG cells do not display cilia or IFT88 (middle). Both overview and magnified single cells are shown. Scale bar 10 μm. At least 500 cells from n = 3 independent experiments were examined.

(C) Experimental set up of Shh signaling activation with SAG. In healthy NPCs, SMO (red) is restricted to basal bodies. On SAG addition, SMO translocates to primary cilia (top panel). Similar to healthy NPCs, U3047MG (responder) lines induced with cilia, but not U3024MG (non-responder) lines, display SMO translocation to newly induced cilia (red, bottom panel). Cilia are labeled with Arl13B (green). Naive U3047MG cells do not show cilia, and thus SMO is restricted to basal bodies (middle panel). Scale bar, 5 μm. Bar diagram at right quantifies fractions of cells whose cilia respond to SAG activation. At least 200 cells from n = 3 independent experiments were tested. Ordinary two-way ANOVA followed by Sidak's multiple comparisons test ***$p < 0.001$. ns, non-significant. Error bars show mean ± SEM.

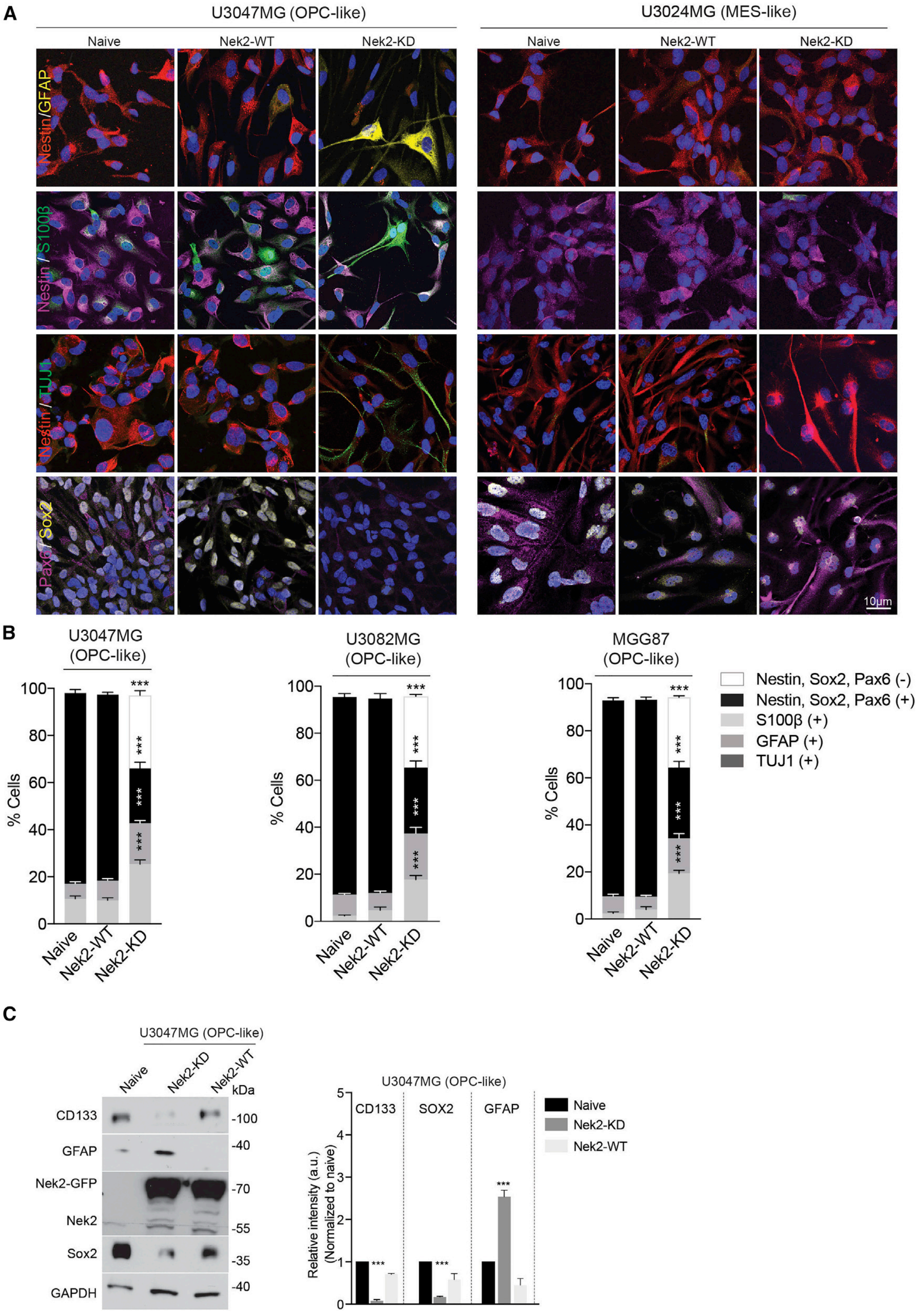

(legend on next page)

U3047MG can play a role in sequestering excessive PDGFR-α (Figure S7G). Supportive of this is our super-resolution imaging assay strikingly indicating the presence of PDGFR-α, mostly in newly induced cilium. Importantly, naive U3047MG cells that have suppressed ciliogenesis exhibited unspecific localization of PDGFR-α nearly the entire cell's space suggesting that cilium induction switches PDGFR-α to be relocated to a newly induced cilium (Figure S7H).

From these findings, we reasoned that the upregulated total PDGFR-α in GSCs is constitutively active in ligand-independent manner, which could enable them to continuously self-renew. To test this aspect, we imaged the dynamic localization of PDGFR-α at various time points on its activation by its endogenous ligand PDGF-AA (Figure S8). In control experiments that used healthy NPCs, we detected the appearance of PDGFR-α signal in cilia 20 mins after the ligand addition (top panel). In contrast, un-ciliated U3047MG cells always displayed excessive PDGFR-α immunoreactivity in a ligand-independent manner (middle panel). Strikingly, after cilium induction, U3047MG cells showed PDGFR-α dynamics similar to healthy NPCs such that PDGFR-α is directed to a newly induced cilium (bottom panel). In summary, these results elucidate the dominant effect of cilium induction in triggering differentiation of GSCs via regulating abnormally functioning PDGFR-α signaling.

Cilium induction impairs GSCs invasion into 3D human brain organoids and mouse brain

To analyze the impact of cilium induction in GSCs invasion in 3D, we adapted our recently optimized brain organoid-based GSCs invasion assays, which recapitulate some of the *in vivo* behavior of GSCs (Mariappan et al., 2021; Goranci-Buzhala et al., 2020; Linkous et al., 2019). In our assays, we seeded 1,000 naive and Nek2-KD-expressing U3047MG cells at the vicinity of 10-day-old organoids, differentiated from transgenic iPSCs expressing tubulin-GFP. For visualization purposes, GSCs were tagged with mCherry reporter (Figure 7A). After 24 h of seeding, we added doxycycline to induce Nek2-KD protein expression and live-imaged the invasion behavior of GSCs at various time points from days 1–7. Imaging at bright field, we noticed that on day 2, GSCs were attracted to brain organoids. On day 7, a significant proportion of naive GSCs have invaded the organoids. Strikingly, Nek2-KD-expressing GSCs failed to enter brain organoids. In contrast, the non-responder control U3024MG, in which Nek2-KD expression did not induce cilia, invaded the organoids (Figure 7B).

To enhance the image quality and quantitatively determine the 3D invasion behavior of GSCs at the later time point of day 20, we utilized our recently described rapid organoid clearing and imaging methods (Goranci-Buzhala et al., 2020). Naive U3047MG cells extensively diffused and recapitulated the known characteristics of invading GSCs, such as establishing protrusion-like processes in the form of microtubes (Osswald et al., 2015). In contrast, Nek2-KD-expressing U3047MG cells exhibited an impaired organoid invasion and, therefore, failed to grow in brain organoids (Figure 7C; Videos S1 and S2).

To determine the fate of Nek2-KD-expressing U3047MG cells in 3D organoids, we performed immunofluorescence imaging of thin-sectioned organoids harboring GSCs invasion. We noticed that Nek2-KD-expressing U3047MG cells, but not naive cells, were strongly positive for GFAP exhibiting characteristic astrocyte-like cell shapes. These findings reveal that Nek2-KD-expressing U3047MG cells underwent a differentiation process similar to what was observed in our 2D experiments on cilium induction (Figure S9). Together, our organoid-based invasion assay elucidates that Nek2-KD expression triggers differentiation of GSCs within brain organoids and thereby impairs their invasion.

To further test if cilium induction can perturb GSCs invasion *in vivo*, we grafted 2×10^4 Nek2-KD-expressing U3047MG cells intracerebrally into immune-deficient mice. This procedure generates infiltrative tumor xenografts closely mimicking the parental tumor's behavior (see STAR Methods for details) (Ricci-Vitiani et al., 2010). To induce cilia via Nek2-KD expression, we supplied animals with doxycycline (1 mg/mL) in drinking water. At week 4 after grafting, control groups that did not drink doxycycline water displayed GSCs along the needle tract spreading onto the corpus callosum and deeper into the striatum. Conversely, experimental groups that drank doxycycline water harbored only a few GSCs at the grafting area. Most of the cells were embedded in cell debris and did not spread further to the corpus callosum and striatum (Figure 7D). Examiningcells for cilium induction revealed that U3047MG cells displayed cilia, which was abnormally long, corroborating that cilium induction can significantly perturb U3047MG invasion *in vivo* (Figure 7E).

DISCUSSION

Glioblastoma constitutes self-renewing, highly tumorigenic GSCs that exhibit striking similarities to NPCs expressing neural stem cell markers, assemble spheres, and rapidly self-renew (Bhaduri et al., 2020; Rajakulendran et al., 2019). Patient-derived GSCs rapidly invade into human brain organoids and mouse brain, assemble invasive networks, and form tumors that

Figure 5. Cilium induction triggers GSCs differentiation

(A) Naive or Nek2-WT-expressing U3047MG GSCs (responder) display neural stem cell marker Nestin (red), Pax6 (magenta), and Sox2 (yellow) but not differentiation markers of GFAP, S100β, and TUJ-1 (left and middle panel). These GSCs lose neural stem cell markers on cilium induction but gain differentiation markers of GFAP, S100β, and TUJ1. Non-responder line (U3024MG), in contrast, neither differentiates nor loses its stem cell markers.

(B) Bar diagram below quantifies fractions of OPC-like GSCs (U3047MG, U3082MG, and MGG87) positive for stemness (Nestin, Sox2, and Pax6) and differentiation (GFAP and TUJ1) markers. At least 200 cells in each cell line from n = 3 independent experiments were analyzed. Ordinary two-way ANOVA followed by Tukey's multiple comparisons test ***$p < 0.001$. Error bars show mean ± SEM.

(C) Western blot compares relative levels of stemness (CD133 and Sox2) and differentiation marker (GFAP) before and after cilium induction. GAPDH was used as a loading control. Bar diagram at right quantifies relative intensities of respective markers before and after cilium induction. Western blots from n = 3 independent experiments. Ordinary two-way ANOVA followed by Tukey's multiple comparisons test, ***$p < 0.001$. Error bars show mean ± SEM.

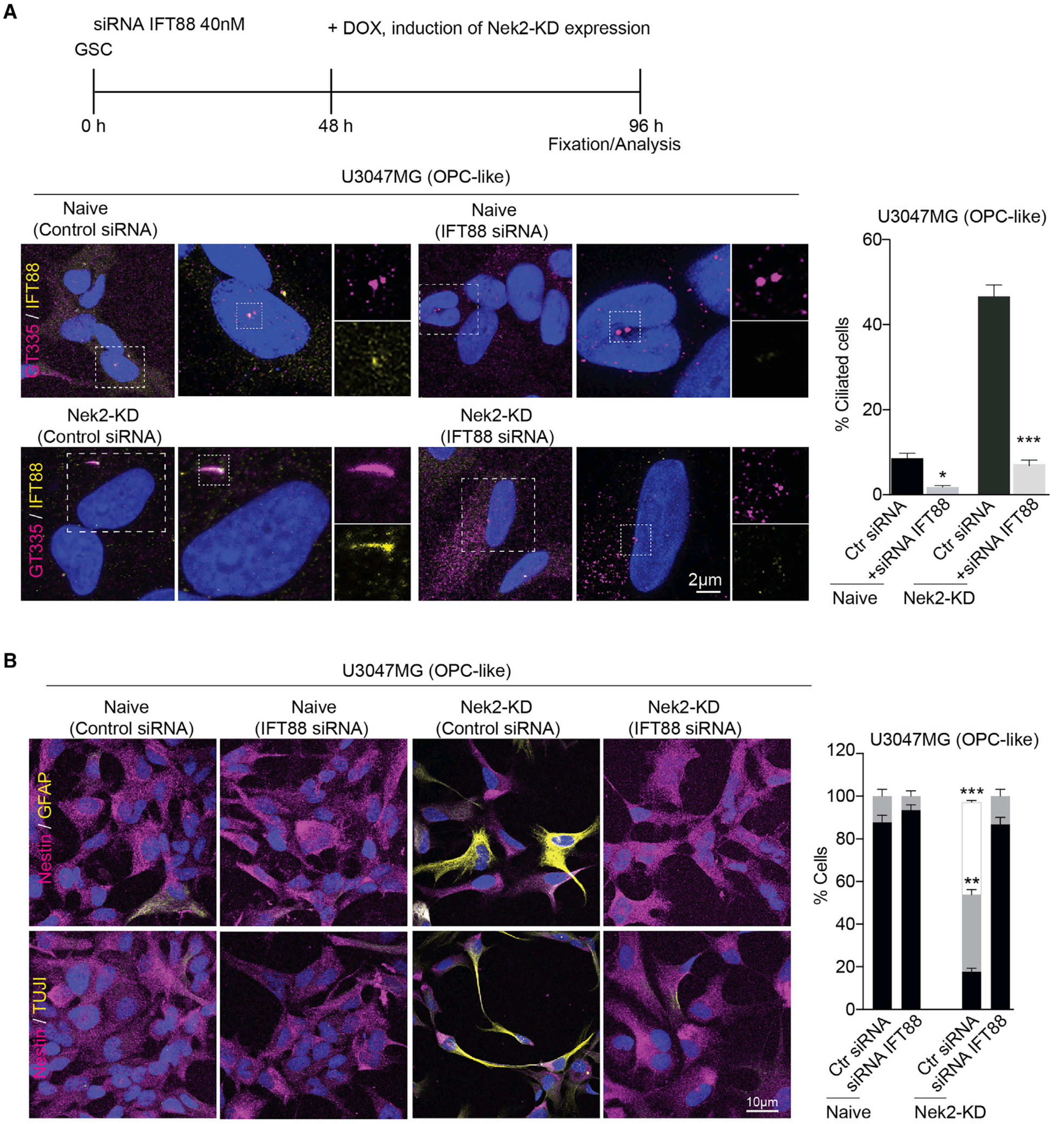

U3047MG (OPC-like)	Treatment	Cilia status	Differentiation (GFAP+ive, TUJ1+ive)
Naive	Control siRNA	Supressed	No
Naive	IFT88 siRNA	Supressed	No
Nek2-KD	Control siRNA	Induced	Yes
Nek2-KD	IFT88 siRNA	Supressed	No

(legend on next page)

phenocopy patient tumors (Mariappan et al., 2021; Goranci-Buzhala et al., 2020; Linkous et al., 2019; Osswald et al., 2015) (Figure 7). Identifying a unique feature of GSCs that strikingly differ from NPCs and exploiting the molecular regulation may provide hints to the development of strategies to selectively impair GSCs proliferation and invasion.

NPCs are functionally characterized by their abilities to self-renew and differentiate. Recently, we and others have identified that the primary cilia are a molecular switch whose spatiotemporal dynamics decisively regulate self-renewal versus differentiation of NPCs (Gabriel et al., 2016; Kim et al., 2011; Li et al., 2011). Delayed cilia disassembly triggers NPCs differentiation, whereas accelerated cilia disassembly promotes NPCs proliferation (Gabriel et al., 2016; Kim et al., 2011; Li et al., 2011). This provides conceptually a novel "cilium checkpoint" that can be targeted to regulate stem cell fate. Although GSCs are strikingly similar to NPCs, GSCs possibly differ in at least two aspects. First, cilium formation is suppressed at the early stages of ciliogenesis due to elevated levels of molecular players (CDC components) that trigger cilia disassembly (Figures 1 and 2). Second, GSCs are characterized by continuous self-renewal and block differentiation (Rajakulendran et al., 2019; Park et al., 2017).

We reasoned that suppressed ciliogenesis might provide a selective advantage to GSCs to continuously self-renew, evading the cell cycle exit and differentiation in a cilium checkpoint-independent manner. It is important to emphasize that cilia loss has a severe consequence in triggering melanoma metastasis by promoting WNT/beta-catenin signaling and resistance development (Zingg et al., 2018, Zhao et al., 2017). Thus, the primary cilium could function as a tumor suppressor organelle in broader cancer types. However, to date, no effort has been made to test the hypothesis of whether re-introducing cilia can be anti-tumorigenic, triggering differentiation of stem cells and impairing their invasion. Therefore, we targeted the cilia disassembly mechanisms of GSCs (Figure S1, hypothesis). Our work identifies that depleting CDC levels act as a mechanism to induce cilia in GSCs persistently. Inducing ciliogenesis in a subset of patient-derived GSCs has triggered them to lose their stemness and gain differentiation programs (Figures 5 and S6). As a result, GSCs induced with cilia failed to invade into 3D human brain organoids and mouse brains (Figure 7).

Recruitment of CDC components to the ciliary base is associated with temporal cilia disassembly at the onset of cell cycle reentry (Gabriel et al., 2016). However, the molecular interplay between CDC recruitment and cilia disassembly remained elusive. It is conceivable that the CDC could contain an enzyme that can be activated to depolymerize the microtubule cytoskeleton of cilia during disassembly. The identification of Kif24, a depolymerizing microtubule kinesin, and Nek2 as components of CDC helps to unveil the mechanisms of CDC-mediated cilia disassembly (Kim et al., 2015). It is noteworthy that Nek2 kinase levels are elevated in naive GSCs that exhibit suppressed ciliogenesis (Figure 2). The depletion of cell-cycle-related kinase has also been shown to induce cilia in a small fraction of serum-starved U251MG cells (Yang et al., 2013). It is noteworthy that, unlike GSCs, the commercially available U251MG cells were cultured in the presence of serum. Thus, it remains unclear whether the small fraction of ciliated cells observed is due to the depletion of kinase or serum starvation.

Inducing ciliogenesis, GSCs behave like NPCs undergoing a differentiation suggesting that newly induced cilia are structurally and functionally normal (Figure 4). This supports the notion that cilia can functionally be restored in a subset of GSCs that are categorized as OPC-like GSCs expressing an elevated level of PDGFR-α. Restoring cilia first sequesters excessive PDGFR-α into newly induced cilia and resets aberrant PDGFR-α signaling (Figures S7G and S7H). The observed drastic reduction in total PDGFR-α levels after cilium induction is a surprising phenomenon suggesting that cilia could harbor proteasomal subunit components to degrade newly translocated ciliary PDGFR-α. Interestingly, at least three components of 19S proteasomal subunits have been identified in mouse embryonic fibroblast cilia (Gerhardt et al., 2015). It is thus tempting to investigate if cilia of NPCs and GSCs harbor proteasomal subunits and E3 ligases that can recognize PDGFR-α and critically regulate its amount and downstream signaling.

PDFGRA signaling is mediated by the primary cilium (Schneider et al., 2005). Of note, expressing Nek2-KD sensitized only PDGFR-α overexpressing OPC-like GSCs but not other subtypes. There could be several reasons for this selectivity. Compared to other CDC components, OPC-like GSCs (responder lines) express the highest level of Nek2 (Figures 2A and 2B). Second, it is possible that OPC-like GSCs (that exhibit an increased level of PDGFRA) still harbor cilium induction programs that are perhaps masked in other cellular states. Finally, PDGFR-α overexpressing GSCs may harbor epigenetically regulated neurogenic and astrogenic features. Thus, restoring ciliogenesis could favor differentiation and loss of self-renewal. For example, the transcription factor ASCL1 in OPC-like (pro-neural subtypes) GSCs has been shown to unlock chromatin allowing new sites to activate differentiation programs (Park et al., 2017). Interestingly, we noticed that the responder

Figure 6. GSCs differentiation is cilium-dependent

(A) Experimental plan. Nek2-KD expression does not induce cilia in GSCs depleted of IFT88. Note Nek2-KD could induce cilia only in control siRNA-treated naive GSCs cultures in which IFT88 immunoreactivity (yellow) is intact (left, both overview and magnified insets are shown). Cilia are labeled with glutamylated tubulin (magenta). In contrast, Nek2-KD does not induce cilia in IFT88-depleted cultures (right, both overview and magnified insets are shown). Note that IFT88 expression is lost. Scale bar, 2 μm. Bar diagram at right quantifies frequencies of ciliated cells under various conditions tested. At least 300 cells were tested from n = 3 experiments. Ordinary one-way ANOVA followed by Tukey's multiple comparisons test. ***$p < 0.001$, *$p < 0.05$. Error bars show mean ± SEM.

(B) Nek2-KD expression triggers differentiation (GFAP- and TUJ1-positive cells) only in control siRNA-treated cells where Nek2-KD could induce cilia (refer to the previous experiment). Thus, Nek2-KD-mediated GSCs differentiation is cilium-dependent. Note that IFT88 depletion or control siRNA alone does not trigger GSCs differentiation (second and first panel from left). With the exception of Nek2-KD-expressing control siRNA-treated cultures, the rest of the cultures exhibit neural stem cell marker Nestin. Scale bar, 10 μm. At least 100 cells were tested from n = 3 experiments. Ordinary two-way ANOVA followed by Tukey's multiple comparisons test. ***$p < 0.001$, **$p < 0.01$. Error bars show mean ± SEM. The table summarizes the experimental results.

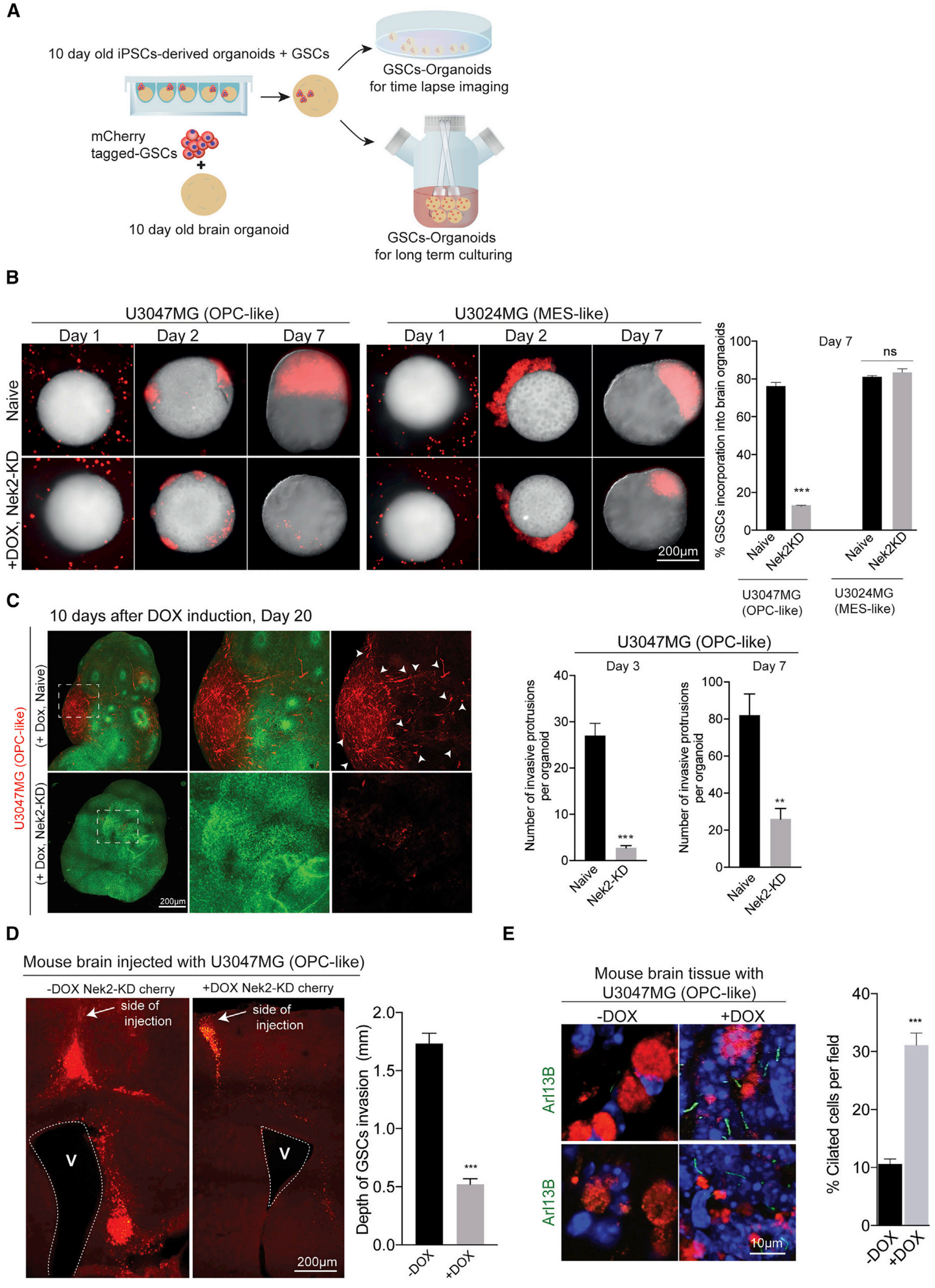

(legend on next page)

line (U3047MG) does quantitatively express a higher ASCL1 expression than the non-responder line (U3024MG) (data not shown). Recent work has also uncovered an elevated level of EZH2, a polycomb repressive complex 2, as a mechanism by which cancer cells lose cilia and promote metastatic melanoma (Zingg et al., 2018). Future experiments with detailed transcriptomic and systems analysis will uncover yet unknown epigenetic factors that mask cilium induction and differentiation in a wide variety of GSCs. It will be also interesting to test a hypothesis whether introducing PDGFRA in non-responder GSCs will enable cilium induction or depleting PDGFRA in responder GSCs will make them non-responders.

Currently, it remains unknown why cilium induction was not possible in non-responder of AC-like and MES-like lines. The non-responder lines may likely harbor defective centrioles, which will not assemble cilia at all. Thus, a comprehensive analysis of centriole, basal body, and cilia structure is required. Second, it is unknown whether there are mutations in cilia inducing genes and if they are under epigenetic regulation. Finally, it remains unknown if ciliary microtubule polymerases (such as Kif24) are constitutively active in non-responder lines.

In summary, as a cellular organelle that regulates signaling, self-renewal, and differentiation, the cilium checkpoint emerges as an attractive molecular switch that can be targeted to alter the fundamental aspects of GSCs. Identification of CDC components and their elevated levels coupled with suppressed ciliogenesis begins to explain why GSCs tend to continuously self-renew and invade the brain. Cilium-induced differentiation in GSCs has a broader impact on 3D brain organoids, which has recently received considerable attention as a human *in vitro* system to evaluate GSCs invasion and glioma-neuron interaction (Linkous et al., 2019; Goranci-Buzhala et al., 2020). As shown in our organoid-based invasion assays and mouse xenografts, invasive protrusions formed by naive GSCs were completely abrogated on cilium induction (Figure 7). Therefore, the perturbed GSC invasion observed in brain organoids and mouse brain suggests that targeting CDC, cilium checkpoint including enzymes that deconstruct cilia, emerge as “Achilles’ heel” to limit GSCs invasion.

STAR★METHODS

Detailed methods are provided in the online version of this paper and include the following:

- KEY RESOURCES TABLE
- RESOURCE AVAILABILITY
  - Lead contact
  - Materials availability
  - Data and code availability
- EXPERIMENTAL MODEL AND SUBJECT DETAILS
  - Primary GSCs isolation from GBMs
  - Culturing and maintenance of patient-derived GSCs
  - Primary GSCs and GBM tissues used
  - Intracranial xenografts of human GSCs in mouse
- METHOD DETAILS
  - Plasmids and cloning
  - Real-time quantitative PCR
  - Lentiviral production and transduction of target cells
  - Culturing and maintenance of human iPSC culture
  - Astrocyte generation from NPCs
  - Depletion of IFT88 by siRNA
  - Immunofluorescence microscopy and imaging of organoids
  - Immunohistochemistry on patient-derived GSCs
  - GSCs invasion into brain organoid
  - Whole organoid tissue clearing
  - Fluorescence microscopy and immunofluorescence of brain tumor xenografts
  - Immunohistochemistry on human specimens
  - Electron microscopy
  - Western blotting
  - FLAG-immunoprecipitation (IP) for CPAP and Nek2 complexes
  - RNA sequencing and analysis
- QUANTIFICATIONS AND STATISTICAL ANALYSIS

SUPPLEMENTAL INFORMATION

Supplemental information can be found online at https://doi.org/10.1016/j.celrep.2021.109656.

Figure 7. Cilium induction prevents GSCs invasion into 3D human brain organoids and mouse brain

(A) Experimental scheme showing the process of GSCs invasion assay. Co-culturing of labeled GSCs with 10-day-old brain organoids until imaging them.

(B) Bright-field images show that mCherry-tagged OPC-like U3047MG and MES-like U3024MG cells (top panel) invasion into 3D human brain organoids. On Nek2-KD induction, OPC-like U3047MG cells (bottom left) exhibit impaired invasion but not MES-like U3024MG cells (bottom right). In these experiments, untagged iPSCs were used to generate brain organoids. Scale bar, 200 μm. At least 20 organoids from 5 different batches were tested. Ordinary two-way ANOVA followed by Tukey’s multiple comparisons test $***p < 0.001$. ns, non-significant. Error bars show mean ± SEM.

(C) Tissue-cleared 3D imaging of the whole organoid after 20 days of GSCs invasion. Tissue clearing enhances the visualization of U3047MG-mCherry growth (red) into the organoids (green). Invading GSCs form protrusions and microtube networks (top panel). In contrast, Nek2-KD-expressing U3047MG cells grow poorly within organoids, as evidenced by poor growth and less intensity (bottom panel). The bar graph at right quantifies the parameters of invasiveness before and after cilium induction. Unpaired t test, $***p < 0.001$, $**p < 0.01$. Error bars show mean ± SEM.

(D) Mouse brains at 4 weeks after grafting m-Cherry-tagged U3047MG cells expressing Nek2-KD. Coronal sections of the grafted brains are shown. The control animal groups that do not drink doxycycline (−DOX) water exhibit invading GSCs deep into the striatum. In contrast, coronal sections of the animal groups that drank doxycycline (+DOX) exhibit an impaired invasion or migration of GSCs. The arrow marks the site of GSCs injection. Dotted lines mark ventricles (V). Scale bar, 200 μm. At right, bar diagram quantifies depth of GSCs invasion between control (that did not drink doxycycline, −DOX) and experimental (that did drink doxycycline, +DOX) animal groups. At least ten sections per animal were analyzed from $n = 4$ (control group) and $n = 5$ (experimental group) animals. Unpaired t test. $***p < 0.001$. Error bars show mean ± SEM.

(E) Immunofluorescence analysis of cilia. GSCs at the control group (that did not drink doxycycline, −DOX) do not show cilia. In contrast, GSCs at the experimental animal groups (that did drink doxycycline, +DOX), show newly induced cilia (green). At least ten sections per animal were analyzed from $n = 4$ (control group) and $n = 5$ (experimental group) animals. Scale bar, 10 μm. Unpaired t test. $***p < 0.001$. Error bars show mean ± SEM.

ACKNOWLEDGMENT

We thank the members of the Laboratory for Centrosome and Cytoskeleton Biology and the Institute of Human Genetics for their support. We thank Dr. Hiroaki Wakimoto for offering GSCs (MGG87, MGG8). We thank Abida Pranty Islam for helping with biochemical experiments. We thank Prof. Karin Forsberg-Nilson for providing patient-derived GBM cells, which were acquired from the Human Glioblastoma Cell Culture resource (https://www.hgcc.se) at the Department of Immunology, Genetics and Pathology, Uppsala University, Sweden. We want to thank Mrs. A. Hermansson for her excellent technical assistance with GBM cells. This work is supported by Deutsche Krebshilfe (70114276). R.P. is supported by AIRC (IG 2019 Id.23154), and N.J. and A.P. are supported by SPP1935. G.G.-B. was supported by the Pharmacology and Bayer Graduate Program at the University of Cologne.

AUTHOR CONTRIBUTIONS

J.G., A.M., and G.G.-B. conceived the project concept. G.G.-B. performed most of the experiments. J.G. supervised the work. A.M. performed super-resolution, organoid imaging and shRNA-mediated CDC depletion. G.C. and M.G. performed electron microscopy analyses. A.P. and N.J. performed RNA transcriptomic analyses. J.G. wrote the manuscript. Input was provided by all authors.

DECLARATION OF INTERESTS

The authors declare no competing interests.

Received: March 6, 2020
Revised: June 17, 2021
Accepted: August 12, 2021
Published: September 7, 2021

REFERENCES

Anvarian, Z., Mykytyn, K., Mukhopadhyay, S., Pedersen, L.B., and Christensen, S.T. (2019). Cellular signalling by primary cilia in development, organ function and disease. Nat. Rev. Nephrol. *15*, 199–219.

Bangs, F., and Anderson, K.V. (2017). Primary Cilia and Mammalian Hedgehog Signaling. Cold Spring Harb. Perspect. Biol. *9*, a028175.

Bhaduri, A., Di Lullo, E., Jung, D., Müller, S., Crouch, E.E., Espinosa, C.S., Ozawa, T., Alvarado, B., Spatazza, J., Cadwell, C.R., et al. (2020). Outer Radial Glia-like Cancer Stem Cells Contribute to Heterogeneity of Glioblastoma. Cell Stem Cell *26*, 48–63.e6.

Brennan, C.W., Verhaak, R.G., McKenna, A., Campos, B., Noushmehr, H., Salama, S.R., Zheng, S., Chakravarty, D., Sanborn, J.Z., Berman, S.H., et al.; TCGA Research Network (2013). The somatic genomic landscape of glioblastoma. Cell *155*, 462–477.

Chan, K.M., Fang, D., Gan, H., Hashizume, R., Yu, C., Schroeder, M., Gupta, N., Mueller, S., James, C.D., Jenkins, R., et al. (2013). The histone H3.3K27M mutation in pediatric glioma reprograms H3K27 methylation and gene expression. Genes Dev *27*, 985–990.

Clarke, I.D., and Dirks, P.B. (2003). A human brain tumor-derived PDGFR-alpha deletion mutant is transforming. Oncogene *22*, 722–733.

D'Alessandris, Q.G., Biffoni, M., Martini, M., Runci, D., Buccarelli, M., Cenci, T., Signore, M., Stancato, L., Olivi, A., De Maria, R., et al. (2017). The clinical value of patient-derived glioblastoma tumorspheres in predicting treatment response. Neuro-oncol. *19*, 1097–1108.

Đặng, T.C., Ishii, Y., Nguyen, V., Yamamoto, S., Hamashima, T., Okuno, N., Nguyen, Q.L., Sang, Y., Ohkawa, N., Saitoh, Y., et al. (2019). Powerful Homeostatic Control of Oligodendroglial Lineage by PDGFRα in Adult Brain. Cell Rep. *27*, 1073–1089.e5.

Dobin, A., Davis, C.A., Schlesinger, F., Drenkow, J., Zaleski, C., Jha, S., Batut, P., Chaisson, M., and Gingeras, T.R. (2013). STAR: ultrafast universal RNA-seq aligner. Bioinformatics *29*, 15–21.

Fabbri, L., Bost, F., and Mazure, N.M. (2019). Primary Cilium in Cancer Hallmarks. Int. J. Mol. Sci. *20*, 1336.

Ferreri, A.J., Illerhaus, G., Zucca, E., and Cavalli, F.; International Extranodal Lymphoma Study Group (2010). Flows and flaws in primary central nervous system lymphoma. Nat. Rev. Clin. Oncol. *7*, 10 1038/nrclinonc.

Filbin, M.G., Tirosh, I., Hovestadt, V., Shaw, M.L., Escalante, L.E., Mathewson, N.D., Neftel, C., Frank, N., Pelton, K., Hebert, C.M., et al. (2018). Developmental and oncogenic programs in H3K27M gliomas dissected by single-cell RNA-seq. Science *360*, 331–335.

Fry, A.M., Schultz, S.J., Bartek, J., and Nigg, E.A. (1995). Substrate specificity and cell cycle regulation of the Nek2 protein kinase, a potential human homolog of the mitotic regulator NIMA of Aspergillus nidulans. J. Biol. Chem. *270*, 12899–12905.

Gabriel, E., and Gopalakrishnan, J. (2017). Generation of iPSC-derived Human Brain Organoids to Model Early Neurodevelopmental Disorders. J. Vis. Exp. (*122*), 55372.

Gabriel, E., Wason, A., Ramani, A., Gooi, L.M., Keller, P., Pozniakovsky, A., Poser, I., Noack, F., Telugu, N.S., Calegari, F., et al. (2016). CPAP promotes timely cilium disassembly to maintain neural progenitor pool. EMBO J. *35*, 803–819.

Gabriel, E., Ramani, A., Karow, U., Gottardo, M., Natarajan, K., Gooi, L.M., Goranci-Buzhala, G., Krut, O., Peters, F., Nikolic, M., et al. (2017). Recent Zika Virus Isolates Induce Premature Differentiation of Neural Progenitors in Human Brain Organoids. Cell Stem Cell *20*, 397–406.e5.

Gerhardt, C., Lier, J.M., Burmühl, S., Struchtrup, A., Deutschmann, K., Vetter, M., Leu, T., Reeg, S., Grune, T., and Rüther, U. (2015). The transition zone protein Rpgrip1l regulates proteasomal activity at the primary cilium. J. Cell Biol. *210*, 115–133.

Goetz, S.C., Ocbina, P.J., and Anderson, K.V. (2009). The primary cilium as a Hedgehog signal transduction machine. Methods Cell Biol. *94*, 199–222.

Gopalakrishnan, J., Mennella, V., Blachon, S., Zhai, B., Smith, A.H., Megraw, T.L., Nicastro, D., Gygi, S.P., Agard, D.A., and Avidor-Reiss, T. (2011). Sas-4 provides a scaffold for cytoplasmic complexes and tethers them in a centrosome. Nat. Commun. *2*, 359.

Gopalakrishnan, J., Chim, Y.C., Ha, A., Basiri, M.L., Lerit, D.A., Rusan, N.M., and Avidor-Reiss, T. (2012). Tubulin nucleotide status controls Sas-4-dependent pericentriolar material recruitment. Nat. Cell Biol. *14*, 865–873.

Goranci-Buzhala, G., Mariappan, A., Gabriel, E., Ramani, A., Ricci-Vitiani, L., Buccarelli, M., D'Alessandris, Q.G., Pallini, R., and Gopalakrishnan, J. (2020). Rapid and Efficient Invasion Assay of Glioblastoma in Human Brain Organoids. Cell Rep. *31*, 107738.

Haag, D., Mack, N., Benites Goncalves da Silva, P., Statz, B., Clark, J., Tanabe, K., Sharma, T., Jäger, N., Jones, D.T.W., Kawauchi, D., et al. (2021). H3.3-K27M drives neural stem cell-specific gliomagenesis in a human iPSC-derived model. Cancer Cell *39*, 407–422.e13.

Inaba, H., Goto, H., Kasahara, K., Kumamoto, K., Yonemura, S., Inoko, A., Yamano, S., Wanibuchi, H., He, D., Goshima, N., et al. (2016). Ndel1 suppresses ciliogenesis in proliferating cells by regulating the trichoplein-Aurora A pathway. J. Cell Biol. *212*, 409–423.

Jackson, P.K. (2011). Do cilia put brakes on the cell cycle? Nat. Cell Biol. *13*, 340–342.

Jacob, F., Salinas, R.D., Zhang, D.Y., Nguyen, P.T.T., Schnoll, J.G., Wong, S.Z.H., Thokala, R., Sheikh, S., Saxena, D., Prokop, S., et al. (2020). A Patient-Derived Glioblastoma Organoid Model and Biobank Recapitulates Inter- and Intra-tumoral Heterogeneity. Cell *180*, 188–204.e22.

Johnson, D.R., and O'Neill, B.P. (2012). Glioblastoma survival in the United States before and during the temozolomide era. J. Neurooncol. *107*, 359–364.

Kim, S., Zaghloul, N.A., Bubenshchikova, E., Oh, E.C., Rankin, S., Katsanis, N., Obara, T., and Tsiokas, L. (2011). Nde1-mediated inhibition of ciliogenesis affects cell cycle re-entry. Nat. Cell Biol. *13*, 351–360.

Kim, S., Lee, K., Choi, J.H., Ringstad, N., and Dynlacht, B.D. (2015). Nek2 activation of Kif24 ensures cilium disassembly during the cell cycle. Nat. Commun. *6*, 8087.

Klingberg, A., Hasenberg, A., Ludwig-Portugall, I., Medyukhina, A., Männ, L., Brenzel, A., Engel, D.R., Figge, M.T., Kurts, C., and Gunzer, M. (2017). Fully Automated Evaluation of Total Glomerular Number and Capillary Tuft Size in Nephritic Kidneys Using Lightsheet Microscopy. J. Am. Soc. Nephrol. *28*, 452–459.

Kobayashi, T., Tsang, W.Y., Li, J., Lane, W., and Dynlacht, B.D. (2011). Centriolar kinesin Kif24 interacts with CP110 to remodel microtubules and regulate ciliogenesis. Cell *145*, 914–925.

Larsen, J., Grigoriev, I., Akhmanova, A., and Pedersen, L.B. (2013). Analysis of microtubule plus-end-tracking proteins in cilia. Methods Enzymol. *524*, 105–122.

Lathia, J.D., Mack, S.C., Mulkearns-Hubert, E.E., Valentim, C.L., and Rich, J.N. (2015). Cancer stem cells in glioblastoma. Genes Dev. *29*, 1203–1217.

Li, A., Saito, M., Chuang, J.Z., Tseng, Y.Y., Dedesma, C., Tomizawa, K., Kaitsuka, T., and Sung, C.H. (2011). Ciliary transition zone activation of phosphorylated Tctex-1 controls ciliary resorption, S-phase entry and fate of neural progenitors. Nat. Cell Biol. *13*, 402–411.

Liao, Y., Smyth, G.K., and Shi, W. (2014). featureCounts: an efficient general purpose program for assigning sequence reads to genomic features. Bioinformatics *30*, 923–930.

Liau, B.B., Sievers, C., Donohue, L.K., Gillespie, S.M., Flavahan, W.A., Miller, T.E., Venteicher, A.S., Hebert, C.H., Carey, C.D., Rodig, S.J., et al. (2017). Adaptive Chromatin Remodeling Drives Glioblastoma Stem Cell Plasticity and Drug Tolerance. Cell Stem Cell *20*, 233–246.e7.

Linkous, A., Balamatsias, D., Snuderl, M., Edwards, L., Miyaguchi, K., Milner, T., Reich, B., Cohen-Gould, L., Storaska, A., Nakayama, Y., et al. (2019). Modeling Patient-Derived Glioblastoma with Cerebral Organoids. Cell Rep. *26*, 3203–3211.e5.

Loskutov, Y.V., Griffin, C.L., Marinak, K.M., Bobko, A., Margaryan, N.V., Geldenhuys, W.J., Sarkaria, J.N., and Pugacheva, E.N. (2018). LPA signaling is regulated through the primary cilium: a novel target in glioblastoma. Oncogene *37*, 1457–1471.

Love, M.I., Huber, W., and Anders, S. (2014). Moderated estimation of fold change and dispersion for RNA-seq data with DESeq2. Genome Biol. *15*, 550.

Mariappan, A., Goranci-Buzhala, G., Ricci-Vitiani, L., Pallini, R., and Gopalakrishnan, J. (2021). Trends and challenges in modeling glioma using 3D human brain organoids. Cell Death Differ. *28*, 15–23.

Marziali, G., Buccarelli, M., Giuliani, A., Ilari, R., Grande, S., Palma, A., D'Alessandris, Q.G., Martini, M., Biffoni, M., Pallini, R., and Ricci-Vitiani, L. (2017). A three-microRNA signature identifies two subtypes of glioblastoma patients with different clinical outcomes. Mol. Oncol. *11*, 1115–1129.

Matsukado, Y., MacCarty, C.S., and Kernohan, J.W. (1961). The growth of glioblastoma multiforme (astrocytomas, grades 3 and 4) in neurosurgical practice. J. Neurosurg. *18*, 636–644.

Moser, J.J., Fritzler, M.J., and Rattner, J.B. (2009). Primary ciliogenesis defects are associated with human astrocytoma/glioblastoma cells. BMC Cancer *9*, 448.

Moser, J.J., Fritzler, M.J., and Rattner, J.B. (2014). Ultrastructural characterization of primary cilia in pathologically characterized human glioblastoma multiforme (GBM) tumors. BMC Clin. Pathol. *14*, 40.

Nachury, M.V., and Mick, D.U. (2019). Establishing and regulating the composition of cilia for signal transduction. Nat. Rev. Mol. Cell Biol. *20*, 389–405.

Neftel, C., Laffy, J., Filbin, M.G., Hara, T., Shore, M.E., Rahme, G.J., Richman, A.R., Silverbush, D., Shaw, M.L., Hebert, C.M., et al. (2019). An Integrative Model of Cellular States, Plasticity, and Genetics for Glioblastoma. Cell *178*, 835–849.e21.

Osswald, M., Jung, E., Sahm, F., Solecki, G., Venkataramani, V., Blaes, J., Weil, S., Horstmann, H., Wiestler, B., Syed, M., et al. (2015). Brain tumour cells interconnect to a functional and resistant network. Nature *528*, 93–98.

Ostrom, Q.T., Bauchet, L., Davis, F.G., Deltour, I., Fisher, J.L., Langer, C.E., Pekmezci, M., Schwartzbaum, J.A., Turner, M.C., Walsh, K.M., et al. (2014). The epidemiology of glioma in adults: a "state of the science" review. Neuro-oncol. *16*, 896–913.

Park, N.I., Guilhamon, P., Desai, K., McAdam, R.F., Langille, E., O'Connor, M., Lan, X., Whetstone, H., Coutinho, F.J., Vanner, R.J., et al. (2017). ASCL1 Reorganizes Chromatin to Direct Neuronal Fate and Suppress Tumorigenicity of Glioblastoma Stem Cells. Cell Stem Cell *21*, 411.

Pathania, M., De Jay, N., Maestro, N., Harutyunyan, A.S., Nitarska, J., Pahlavan, P., Henderson, S., Mikael, L.G., Richard-Londt, A., Zhang, Y., et al. (2017). H3.3^{K27M} Cooperates with Trp53 Loss and PDGFRA Gain in Mouse Embryonic Neural Progenitor Cells to Induce Invasive High-Grade Gliomas. Cancer Cell *32*, 684–700.e9.

Pine, A.R., Cirigliano, S.M., Nicholson, J.G., Hu, Y., Linkous, A., Miyaguchi, K., Edwards, L., Singhania, R., Schwartz, T.H., Ramakrishna, R., et al. (2020). Tumor Microenvironment Is Critical for the Maintenance of Cellular States Found in Primary Glioblastomas. Cancer Discov. *10*, 964–979.

Pugacheva, E.N., Jablonski, S.A., Hartman, T.R., Henske, E.P., and Golemis, E.A. (2007). HEF1-dependent Aurora A activation induces disassembly of the primary cilium. Cell *129*, 1351–1363.

Rajakulendran, N., Rowland, K.J., Selvadurai, H.J., Ahmadi, M., Park, N.I., Naumenko, S., Dolma, S., Ward, R.J., So, M., Lee, L., et al. (2019). Wnt and Notch signaling govern self-renewal and differentiation in a subset of human glioblastoma stem cells. Genes Dev. *33*, 498–510.

Ricci-Vitiani, L., Pallini, R., Biffoni, M., Todaro, M., Invernici, G., Cenci, T., Maira, G., Parati, E.A., Stassi, G., Larocca, L.M., and De Maria, R. (2010). Tumour vascularization via endothelial differentiation of glioblastoma stem-like cells. Nature *468*, 824–828.

Risso, D., Ngai, J., Speed, T.P., and Dudoit, S. (2014). Normalization of RNA-seq data using factor analysis of control genes or samples. Nat. Biotechnol. *32*, 896–902.

Rivers, L.E., Young, K.M., Rizzi, M., Jamen, F., Psachoulia, K., Wade, A., Kessaris, N., and Richardson, W.D. (2008). PDGFRA/NG2 glia generate myelinating oligodendrocytes and piriform projection neurons in adult mice. Nat. Neurosci. *11*, 1392–1401.

Salomonis, N., Schlieve, C.R., Pereira, L., Wahlquist, C., Colas, A., Zambon, A.C., Vranizan, K., Spindler, M.J., Pico, A.R., Cline, M.S., et al. (2010). Alternative splicing regulates mouse embryonic stem cell pluripotency and differentiation. Proc. Natl. Acad. Sci. USA *107*, 10514–10519.

Schmid, F.M., Schou, K.B., Vilhelm, M.J., Holm, M.S., Breslin, L., Farinelli, P., Larsen, L.A., Andersen, J.S., Pedersen, L.B., and Christensen, S.T. (2018). IFT20 modulates ciliary PDGFRα signaling by regulating the stability of Cbl E3 ubiquitin ligases. J. Cell Biol. *217*, 151–161.

Schmidt, A., Chakravarty, A., Brommer, E., Fenne, B.D., Siebler, T., De Meyts, P., and Kiess, W. (2002). Growth failure in a child showing characteristics of Seckel syndrome: possible effects of IGF-I and endogenous IGFBP-3. Clin. Endocrinol. (Oxf.) *57*, 293–299.

Schneider, L., Clement, C.A., Teilmann, S.C., Pazour, G.J., Hoffmann, E.K., Satir, P., and Christensen, S.T. (2005). PDGFRalphaalpha signaling is regulated through the primary cilium in fibroblasts. Curr. Biol. *15*, 1861–1866.

Schou, K.B., Pedersen, L.B., and Christensen, S.T. (2015). Ins and outs of GPCR signaling in primary cilia. EMBO Rep. *16*, 1099–1113.

Seeley, E.S., and Nachury, M.V. (2009). Constructing and deconstructing roles for the primary cilium in tissue architecture and cancer. Methods Cell Biol. *94*, 299–313.

Shi, Y., Kirwan, P., and Livesey, F.J. (2012). Directed differentiation of human pluripotent stem cells to cerebral cortex neurons and neural networks. Nat. Protoc. *7*, 1836–1846.

Singh, S.K., Clarke, I.D., Terasaki, M., Bonn, V.E., Hawkins, C., Squire, J., and Dirks, P.B. (2003). Identification of a cancer stem cell in human brain tumors. Cancer Res. *63*, 5821–5828.

Singh, S.K., Hawkins, C., Clarke, I.D., Squire, J.A., Bayani, J., Hide, T., Henkelman, R.M., Cusimano, M.D., and Dirks, P.B. (2004). Identification of human brain tumour initiating cells. Nature *432*, 396–401.

Stewart, S.A., Dykxhoorn, D.M., Palliser, D., Mizuno, H., Yu, E.Y., An, D.S., Sabatini, D.M., Chen, I.S., Hahn, W.C., Sharp, P.A., et al. (2003). Lentivirus-delivered stable gene silencing by RNAi in primary cells. RNA *9*, 493–501.

Stupp, R., Mason, W.P., van den Bent, M.J., Weller, M., Fisher, B., Taphoorn, M.J., Belanger, K., Brandes, A.A., Marosi, C., Bogdahn, U., et al.; European Organisation for Research and Treatment of Cancer Brain Tumor and Radiotherapy Groups; National Cancer Institute of Canada Clinical Trials Group (2005). Radiotherapy plus concomitant and adjuvant temozolomide for glioblastoma. N. Engl. J. Med. *352*, 987–996.

Suvà, M.L., Rheinbay, E., Gillespie, S.M., Patel, A.P., Wakimoto, H., Rabkin, S.D., Riggi, N., Chi, A.S., Cahill, D.P., Nahed, B.V., et al. (2014). Reconstructing and reprogramming the tumor-propagating potential of glioblastoma stem-like cells. Cell *157*, 580–594.

Tang, Z., Lin, M.G., Stowe, T.R., Chen, S., Zhu, M., Stearns, T., Franco, B., and Zhong, Q. (2013). Autophagy promotes primary ciliogenesis by removing OFD1 from centriolar satellites. Nature *502*, 254–257.

Verhaak, R.G., Hoadley, K.A., Purdom, E., Wang, V., Qi, Y., Wilkerson, M.D., Miller, C.R., Ding, L., Golub, T., Mesirov, J.P., et al.; Cancer Genome Atlas Research Network (2010). Integrated genomic analysis identifies clinically relevant subtypes of glioblastoma characterized by abnormalities in PDGFRA, IDH1, EGFR, and NF1. Cancer Cell *17*, 98–110.

Wang, G., Chen, Q., Zhang, X., Zhang, B., Zhuo, X., Liu, J., Jiang, Q., and Zhang, C. (2013). PCM1 recruits Plk1 to the pericentriolar matrix to promote primary cilia disassembly before mitotic entry. J. Cell Sci. *126*, 1355–1365.

Wang, L., Babikir, H., Müller, S., Yagnik, G., Shamardani, K., Catalan, F., Kohanbash, G., Alvarado, B., Di Lullo, E., Kriegstein, A., et al. (2019). The Phenotypes of Proliferating Glioblastoma Cells Reside on a Single Axis of Variation. Cancer Discov. *9*, 1708–1719.

Xie, Y., Bergström, T., Jiang, Y., Johansson, P., Marinescu, V.D., Lindberg, N., Segerman, A., Wicher, G., Niklasson, M., Baskaran, S., et al. (2015). The Human Glioblastoma Cell Culture Resource: Validated Cell Models Representing All Molecular Subtypes. EBioMedicine *2*, 1351–1363.

Yang, Y., Roine, N., and Mäkelä, T.P. (2013). CCRK depletion inhibits glioblastoma cell proliferation in a cilium-dependent manner. EMBO Rep. *14*, 741–747.

Zhao, X., Pak, E., Ornell, K.J., Pazyra-Murphy, M.F., MacKenzie, E.L., Chadwick, E.J., Ponomaryov, T., Kelleher, J.F., and Segal, R.A. (2017). A transposon screen identifies loss of primary cilia as a mechanism of resistance to Smo inhibitors. Cancer Discov. *7*, 1436–1449.

Zingg, D., Debbache, J., Peña-Hernández, R., Antunes, A.T., Schaefer, S.M., Cheng, P.F., Zimmerli, D., Haeusel, J., Calçada, R.R., Tuncer, E., et al. (2018). EZH2-Mediated Primary Cilium Deconstruction Drives Metastatic Melanoma Formation. Cancer Cell *34*, 69–84.e14.

STAR★METHODS

KEY RESOURCES TABLE

REAGENT or RESOURCE	SOURCE	IDENTIFIER
Antibodies		
Mouse Anti-gamma-Tubulin Monoclonal Antibody, Unconjugated, Clone GTU-88	Sigma-Aldrich	Cat# T6557; RRID:AB_477584
Rabbit polyclonal anti- Arl13B	Proteintech	Cat# 17711-1-AP; RRID:AB_2060867
Mouse monoclonal anti-Arl13B	NeuroMab, Davis, CA, USA	Cat# 73-287; RRID:AB_11000053
Mouse monoclonal anti-Acetylated tubulin	Sigma-Aldrich	Cat# T7451; RRID:AB_609894
Rabbit polyclonal anti-Nde1	Proteintech	Cat# 10233-1-AP; RRID:AB_2149877
Mouse monoclonal anti-Nestin (4D11)	Novus Biologicals	Cat# NBP1-92717SS; RRID:AB_11013546
Rabbit anti-Anti-beta-Tubulin III (Tuj1)	Sigma-Aldrich	Cat# T2200; RRID:AB_262133
Mouse monoclonal anti-Pax6	DSHB	Cat# pax6; RRID:AB_528427
Mouse monoclonal anti-Nek2	BD Biosciences	Cat# 610593; RRID:AB_397933
Rabbit anti-OFD1	Gift from Prof. Jeremy Reiter	N/A
Mouse monoclonal anti-AuroraA (1F8)	Cell Signaling Technology	Cat# 12100; RRID:AB_2797820
Mouse monoclonal anti-HDAC6 (D-11)	Santa Cruz Biotechnology	Cat# sc-28386; RRID:AB_627708
Mouse monoclonal anti-CD133/Prominin-1	DSHB	Cat# CD133 HB#7; RRID:AB_2619580
Mouse monoclonal anti-CD15/SSEA1	DSHB	Cat# MC-480 (SSEA-1); RRID:AB_528475
Mouse monoclonal anti-PDGFR-α (C-9)	Santa Cruz Biotechnology	Cat# sc-398206
Rabbit polyclonal anti-SOX2	Millipore	Cat# AB5603; RRID:AB_2286686
Mouse monoclonal anti-FLAG	Sigma-Aldrich	Cat# F1804; RRID:AB_262044
Rabbit monoclonal anti-GFAP (D14Q)	Cell Signaling Technology	Cat# 47084; RRID:AB_2799321
Rabbit polyclonal anti-N-cadherin	Abcam	Cat# ab18203; RRID:AB_444317
Rabbit monoclonal anti-S100 beta	Abcam	Cat# ab52642; RRID:AB_882426
Mouse monoclonal anti-Polyglutamylation Modification mAb (GT335)	AdipoGen	Cat# AG-20B-0020; RRID:AB_2490210
Rabbit polyclonal anti-IFT88	Proteintech	Cat# 13967-1-AP; RRID:AB_2121979
Mouse monoclonal anti-Ki67	DSHB	Cat# AFFN-KI67-3E6; RRID:AB_2617702
DAPI	Thermo scientific	Cat# 32670; RRID:AB_2629482
Donkey anti rabbit IgG (H+L) secondary antibody, Alexa Fluor 594	Thermo scientific	Cat# A21207; RRID:AB_141637
Donkey anti rabbit IgG (H+L) secondary antibody, Alexa Fluor 647	Thermo scientific	Cat# A31573; RRID:AB_2536183
Donkey anti-Rabbit IgG (H+L) Secondary Antibody, HRP	Thermo scientific	-Cat# A16023; RRID:AB_2534697
Goat anti mouse IgG (H+L) secondary antibody, Alexa Fluor 488	Thermo scientific	Cat# A28175; RRID:AB_2536161
Goat anti mouse IgG (H+L) secondary antibody, Alexa Fluor 594	Thermo scientific	Cat# A11032; RRID:AB_2534091
Goat anti mouse IgG (H+L) secondary antibody, Alexa Fluor 647	Thermo scientific	Cat# A-21236; RRID:AB_2535805
Rat monoclonal anti-Collapsin Response-Mediated Protein 5 (CRMP5)	Millipore	Cat# MAB5442; RRID:AB_240850
Rabbit polyclonal anti-AKT	Cell signaling	Cat# 9272;RRID:AB_329827
Rabbit polyclonal anti-phospho AKT	Cell signaling	Cat# 9271; RRID:AB_329825
Mouse monoclonal anti-CD44	DSHB	Cat# h4c4; RRID:AB_528147
Rabbit polycolonal anti-c-Myc (Y69)	Abcam	Cat# ab32072; RRID:AB_731658

(Continued on next page)

Continued

REAGENT or RESOURCE	SOURCE	IDENTIFIER
Bacterial and virus strains		
NEB® 10-beta Competent *E. coli* (High Efficiency)	NEB	Cat# C3019H
NEB® 5-alpha Competent *E. coli* (High Efficiency)	NEB	Cat# C2987H
Biological samples		
Human glioblastoma brain tissues	University of Rom, Italy (Prof. Roberto Pallini)	N/A
Chemicals, peptides, and recombinant proteins		
Bovine Serum Albumin solution	Sigma-Aldrich	Cat# A9576-50ML, CAS: 0048-46-8
Accutase solution	Sigma-Aldrich	Cat# A6964-100ML
B-27 Supplement (50X), minus vitamin A	GIBCO	Cat# 12587010
bFGF	Peprotech	Cat# 100-18B
Dorsomorphin	Sigma-Aldrich	Cat# P5499, CAS: 866405-64-3
EGF	Peprotech	Cat# 100-15
Ethyl cinnamate	Sigma-Aldrich	Cat# 112372-100G, CAS: 103-36-6
Heparin	Stem cell technologies	Cat# 07980, CAS: 9041-08-1
Insulin	Sigma-Aldrich	Cat# I3536-100MG, CAS: 11061-68-0
L-Glutamin	Thermo scientific	Cat# 25030081, CAS: 56-85-9
Laminin	Sigma-Aldrich	Cat# L2020, CAS: 114956-81-9
Matrigel hESC-qualified matrix	Corning	Cat# 354277
MEM-NEAA	Thermo scientific	Cat# 11140050
mTeSR1	Stem cell technologies	Cat# 05850
N-2 Supplement (100X)	GIBCO	Cat# 17502048
Neural Basal Medium	GIBCO	Cat# 21103049
Neural induction medium (NIM)	Stem cell technologies	Cat# 21103049
Neurocult NS-A basal medium	Stem cell technologies	Cat# 05750
Paraformaldehyde	Applichem	Cat# A3813,1000 CAS: 30525-89-4
PBS tablets	GIBCO	Cat#18912-014
Penicillin-Streptomycin (100x)	Thermo scientific	Cat# 15140-122
Poly-L-ornithine solution	Sigma-Aldrich	Cat# P4957
ReLeSR	Stem cell technologies	Cat# 05872
SB43154	Selleck Chemicals	Cat# S1067, CAS: 301836-41-9
Sucrose	Applichem	Cat# A4734,1000, CAS: 57-50-1
Triton X-100	Applichem	Cat# A13880500
Y-27632	Selleck Chemicals	Cat# S1049, CAS: 129830-38-2
Recombinant human PDGF-AA	R&D systems	Cat# 1055-AA
SAG	Tocris	Cat# 4366, CAS: 912545-86-9
Click-iT EdU Cell Proliferation Kit for Imaging, Alexa Fluor 594 dye	Thermo Scientific	Cat# C10339
Premo FUCCI Cell Cycle Sensor (BacMam 2.0)	Thermo Scientific	Cat# P36238
RNeasy Micro Kit	QIAGEN	Cat# 74004
SuperScript VILO cDNA Synthesis Kit	Thermo Scientific	Cat# 11754050
Applied Biosystems TaqMan Gene Expression Master Mix	Thermo Scientific	Cat# 43-690-16
*Trans*IT-X2® Dynamic Delivery System	Mirus	Cat# MIR 6003
RIPA Lysis Buffer System	Santa Cruz	Cat# sc-24948
Bradford Reagent	Sigma-Aldrich	Cat# B6916
Primocin	Invivogen	Cat# ant-pm-05

(*Continued on next page*)

Continued

REAGENT or RESOURCE	SOURCE	IDENTIFIER
Puromycin	Invivogen	Cat# ant-pr-1
Recombinant Human Heregulin	Peprotech	Cat# 100-03
Recombinant Human IGF-I	Peprotech	Cat# 100-11
Recombinant Human CNTF	Peprotech	Cat# 450-13
Experimental models: cell lines		
Human: iPSCs mEGFP TUBA1B	Coriell	Cat# AICS-0012, RRID:CVCL_IR34
Human: iPSCs mRFP TUBA1B	Coriell	Cat# AICS-0031-035, RRID:CVCL_LK44
Human: iPSCs IMR90	WiCell Research Institute	RRID:CVCL_C436
Patient-Derived Glioma Stem Cells: U3047MG, U3024MG, U3082MG, and U3056MG	Kindly provided by Prof. Prof. Karin Forsberg Nilsson, Upsala University, Sweden	N/A
HEK293T	Sigma-Aldrich	Cat# 12022001, RRID:CVCL_0063
Patient-Derived Glioma Stem Cells: MGG87	Kindly provided by Prof. Hiroaki Wakimoto, Massachusetts General Hospital, USA	N/A
GSC line name		
U3047MG	10.1016/j.ebiom.2015.08.026	N/A
U3082MG	10.1016/j.ebiom.2015.08.026	N/A
#450	This paper	N/A
UG3056MG	10.1016/j.ebiom.2015.08.026	N/A
U3024MG	10.1016/j.ebiom.2015.08.026	N/A
#275	This paper	N/A
GSC tissue name		
#177	This paper	N/A
#180	This paper	N/A
#191	This paper	N/A
#135	This paper	N/A
#156	This paper	N/A
#133	This paper	N/A
#179	This paper	N/A
#166	This paper	N/A
#178	This paper	N/A
Experimental models: organisms/strains		
Immunosuppressed NOD SCID Mouse	Charles River, Milan, Italy	N/A
Oligonucleotides		
siRNA ON-Target plus - SMART pool human IFT88	Dharmacon	Cat# L-012281-01
siRNA ON-Target plus - Control pool Non-targeting	Dharmacon	Cat# D-001810-10-05
Primers for qPCR PDGFRA (Hs00998018_m1)	Thermo Scientific	Cat# 4331182
Primers for qPCR EGFR (Hs01076090_m1)	Thermo Scientific	Cat# 4331182
Primers for CDK4 (Hs00364847_m1)	Thermo Scientific	Cat# 4331182
Primers for NF1 (Hs01035108_m1)	Thermo Scientific	Cat# 4331182
Primers for GAPDH (Hs 02758991_g1)	Thermo Scientific	Cat# 4331182
Recombinant DNA		
pSicoR-Ef1a-mCh-Puro	Salomonis et al., 2010	RRID:Addgene_31845
psPAX2	psPAX2 was a gift from Didier Trono (Addgene plasmid # 12260 ; http://n2t.net/addgene:12260 ; RRID:Addgene_12260)	RRID:Addgene_12260

(*Continued on next page*)

Continued

REAGENT or RESOURCE	SOURCE	IDENTIFIER
pMD2.G	pMD2.G was a gift from Didier Trono (Addgene plasmid # 12259 ; http://n2t.net/addgene:12259 ; RRID:Addgene_12259)	RRID:Addgene_12259
pLIX_403	pLIX_403 was a gift from David Root (Addgene plasmid # 41395 ; http://n2t.net/addgene:41395 ; RRID:Addgene_41395)	RRID:Addgene_41395
pLKO.1 puro	pLKO.1 puro was a gift from Bob Weinberg (Addgene plasmid # 8453 ; http://n2t.net/addgene:8453 ; Stewart et al., 2003	RRID:Addgene_8453
pLIX-NEK2-WT EGFP	This paper	N/A
pLIX-NEK2-KD EGFP	This paper	N/A
pSIN CPAP WT EGFP 3xflag	This paper	N/A
Software and algorithms		
Adobe Illustrator CC 2018	Adobe	RRID:SCR_010279
Adobe Photoshop CC 2018	Adobe	RRID:SCR_014199
GraphPad Prism 7	GraphPad Software	RRID: SCR_002798
Fiji Win64 (ImageJ d 1.47)	Wayne Rasband, NIH, USA	RRID:SCR_002285
Deposited data		
Bulk RNA sequence	This paper	Access number GEO: GSE179439
Other		
CellCarrier Spheroid ULA 96-well Microplates	PerkinElmer	Cat# 6055330
Low adherent plate (Lumox)	Sarstedt	Cat# 94.6077.33
MycoAlert Mycoplasma Detection Kit	Lonza	Cat# LT07-118
Organoid embedding sheet	Stem cell technologies	Cat# 08579
μ-slide Angiogenesis	Ibidi	Cat# 81506
μ-Slide 4 Well	Ibidi	Cat# 80426

RESOURCE AVAILABILITY

Lead contact

Requests for more information, resources, and reagents should be directed to the lead contact, Jay Gopalakrishnan (jay.gopalakrishnan@hhu.de).

Materials availability

All reagents generated in this study are available from the lead contact with a completed materials transfer agreement.

Data and code availability

Bulk RNA (access number GSE179439) data have been deposited at GEO and are publicly available as of the date of publication. Any additional information required to reanalyze the data reported in this paper is available from the lead contact upon request.

EXPERIMENTAL MODEL AND SUBJECT DETAILS

Primary GSCs isolation from GBMs

Primary GSCs from the GBMs were isolated using an established protocol (D'Alessandris et al., 2017; Ricci-Vitiani et al., 2010). In brief, GBM surgical specimens were mechanically dissociated and cultured in DMEM /F12 (GIBCO) medium containing 2 mM glutamine, 0.6% glucose, 9.6 g/mL putrescine, 6.3 ng/mL progesterone, 5.2 ng/mL sodium selenite, 0.025 mg/mL insulin, and 0.1 mg/mL transferrin sodium salt (Sigma-Aldrich), supplemented with 10ng/ml epidermal growth factor (EGF) (Peprotech) and 10ng/ml basic fibroblast growth factor (bFGF) (Peprotech). Typically, GSCs are characterized by forming spheres expressing stem-cell markers, such as CD133, sex-determining region Y-box 2 (Sox2), Musashi, and Nestin. CD133 expression was detected by anti-CD133–phycoerythrin (AC133-PE) antibody or PE-conjugated mouse immunoglobulin (Ig)G1 isotype control antibody (Miltenyi Biotec). The expression of Sox2 was analyzed by PerCP-Cy 5.5 mouse anti-Sox2 or PerCP-Cy 5.5 mouse IgG1 isotype control (Becton Dickinson [BD]). Viable cells were identified using 7-amino actinomycin D (Sigma-Aldrich). Cells were analyzed with a FACSCanto flow cytometer (BD).

Besides sphere formation assay, stemness phenotypes of GSCs were assessed by self-renewal capacity and generation of xenografts that are histologically mimicking the parent tumor. To assess clonogenicity, viable cells were dispensed at different densities in 96-well plates by fluorescence-activated cell sorting (FACS Aria, BD). When required, subtype classification of GSCs was performed with the RT2 Profiler PCR Arrays (QIAGEN) (Marziali et al., 2017). All of the described experiments have been performed low passaged GSC cultures.

Culturing and maintenance of patient-derived GSCs

As previously described, patient-derived GSCs (used in Figure 1) were cultured in Neurocult NS-A basal medium (STEMCELL technologies) supplemented with 10% BSA (STEMCELL technologies), L-Glutamin (GIBCO, 25030081), Heparin (STEMCELL technologies), B27 without vitamin A (GIBCO), N2 (GIBCO), 20ng/ml recombinant human epidermal growth factor (hEGF) (Peprotech), 20ng/ml basic fibroblast growth factor (bFGF) (Peprotech) (Xie et al., 2015) (Marziali et al., 2017). Cells were maintained at 37°C and 5% CO2 on poly-L-ornithine-coated (Sigma) and laminin-coated (Sigma) cell culture dishes. Cells were dissociated using Accutase (Thermo Fisher). GSCs were cultured in stem cell medium as described above and analyzed for expression of stem cell markers such as, Sox2, Pax6, Nestin, and for the absence of differentiation markers such as TUJ1 and GFAP.

In ligand stimulation experiments, cells were stimulated with 20 ng/ml PDGF-AA ligand (R&D Systems) for 10–60 min. To study Shh signaling, the agonist SAG (Tocris) 100nM was used. After treatments, cells were fixed and analyzed for respective markers. To analyze cell proliferation, EdU was pulsed in cells for 24h before fixation and stained according to the manufacturer's instructions (Click-iT EdU assay kit, Life Technologies). To analyze cell cycle stages, we transduced cells with FUCCI baculovirus (Premo FUCCI Cell Cycle Sensor (BacMam 2.0)- Thermo scientific). After 48 h, cells were fixed and analyzed for cell cycle stages.

Primary GSCs and GBM tissues used

GSC line name	Donor age	Gender	Diagnosis	Mutation status
U3047MG	66 years	female	GBM grade IV	PDGFRA, OPC-like
U3082MG	70 years	female	GBM grade IV	PDGFRA, OPC-like
MGG87	70 years	male	GBM grade IV	PDGFRA, OPC-like
#450	76 years	female	GBM grade IV	PDGFRA, OPC-like
UG3056MG	68 years	female	GBM grade IV	EGFR, AC-like
U3024MG	73 years	female	GBM grade IV	NF1, MES-like
#275	58 years	male	GBM grade IV	CDK4, NPC-like
GSC tissue name	Donor age	Gender	Diagnosis	Mutation status
#177	70 years	female	GBM grade IV	IDH wt, EGFRvIII+
#180	72 years	male	GBM grade IV	IDH wt, EGFRvIII+
#191	68 years	female	GBM grade IV	IDH wt, EGFRvIII-
#135	67 years	male	GBM grade IV	IDH wt, EGFRvIII-
#156	77 years	male	GBM grade IV	IDH wt
#133	74 years	female	GBM grade IV	IDH mut, EGFRvIII-
#179	69 years	female	GBM grade IV	IDH wt, EGFRvIII-
#166	71 years	male	GBM grade IV	IDH wt, EGFRvIII+
#178	76 years	female	GBM grade IV	IDH wt, EGFRvIII+

Patient cells were obtained upon approved by the institutional ethics committee (Fondazione Policlinico Gemelli, Rome: Protocol CE 2253, 2018-nov-13, Uppsala EPN permit 2007/353 and its addenda 2013-10-28 and 2016-12-29, Medical faculty of the University of Düsseldorf: Study number: 2018-273). Informed consent was obtained from all donors.

Intracranial xenografts of human GSCs in mouse

Experiments involving animals were approved by the Ethical Committee of the Istituto Superiore di Sanità, Rome (Pr. No. 4701/17). Immunosuppressed NOD SCID mice (male, 20-23 g; Charles River, Milan, Italy) were anesthetized with intraperitoneal injection of diazepam (2 mg/100 g) followed by intramuscular injection of ketamine (4 mg/100 g). Animal skulls were immobilized in a stereotactic head frame and a burr hole was made 2 mm right of the midline and 1 mm anterior to the bregma. The tip of a 10 µl-Hamilton microsyringe was placed at a depth of 3 mm from the dura and 5 µl of PBS containing 2×10^4 of either mCherry expressing U3047MG cells were slowly injected (D'Alessandris et al., 2017; Ricci-Vitiani et al., 2010). The U3047MG cells were engineered to express catalytically inactive Nek2-KD upon doxycycline induction. Solutions containing 1 mg/ml doxycycline hyclate (Sigma-Aldrich, St Louis, MO, USA) and 1% (w/v) sucrose were prepared into tap water and protected from light during experiments. After grafting, the animals were kept under pathogen-free conditions in positive-pressure cabinets (Tecniplast Gazzada, Varese, Italy) and observed daily for neurological signs and body weight. After survivals ranging from 4 to 24 weeks, the mice were deeply anesthetized and transcardially perfused with 0.1 M PBS (pH 7.4) then treated with 4% paraformaldehyde in 0.1 M PBS. The brain was removed and stored in 30% sucrose in PBS for 3 days.

METHOD DETAILS

Plasmids and cloning

For lentiviral transductions, full-length Nek2-WT and Nek2-KD (K32R) were subcloned from pLVX 3xflag plasmid into a lentiviral packing vectors pLenti6.3 and pLIX_403. These constructs contain the hPGK promoter and with C-terminal GFP. The pLVX 3xflag NEK2-WT and pLVX 3xflag NEK2-KD was generously provided the Dynlacht lab (Kim et al., 2015). For immunoprecipitation experiments, GFP-tagged CPAP was subcloned from pSIN CPAP-WT plasmid into a lentiviral vector pSIN containing the CMV promoter and in-frame N-terminal 3xflag tag.

Real-time quantitative PCR

Total RNA was extracted from the patient derived GSCs using RNeasy mini extraction kit (QIAGEN) according to the manufacture's instruction. Equal amounts of the different samples of amplified RNA (1000 ng) were transcribed into cDNA. The reverse transcription (RT) reaction was carried out using SuperScript VILO cDNA Synthesis Kit (Thermo Scientific). Gene expression was measured by performing TaqMan PCR using Gene Expression MasterMix (

Thermo Scientific) for PDGFRA (Hs00998018_m1), EGFR (Hs01076090_m1), CDK4 (Hs00364847_m1), NF1 (Hs01035108_m1) on the 7500 Real-Time PCR System (Applied Biosystems) supplied with 7500 Real-Time software. Gene expression fold changes were calculated using the $\Delta\Delta C_T$ method and GAPDH (Hs 02758991_g1) was used as a housekeeping gene.

Lentiviral production and transduction of target cells

Constitutive overexpression of mCherry U3047MG lentiviral vectors was prepared using pSicoR-Ef1a-mCh-Puro (Addgene plasmid 31845). For GSCs, stable lines generation inducible lentivectors were used pLix_403 Nek2-KD EGFP and pLix_403 Nek2-KD EGFP.

The lentiviral shRNA constructs pLKO.1-puro for CDC components (NDE1, OFD1, HDAC, Nek2) were kindly provided by Dr. Rajalingam. The cloned vectors were packed into lentivirus using second-generation packaging plasmids (pMD2.G and psPAX2). Briefly, target vectors and packaging plasmids were transfected into HEK293T cells using calcium chloride. After 16 h, the medium was changed, and the virus was collected after 8 h. The freshly harvested virus was used to transduce target cells in a 1:1 ratio for 72–96 h.

To generate GSCs lines stably expressing inducible GFP tagged-Nek2-WT and Nek2-KD, pLIX_403 lenti inducible gateway cloning vector (Addgene #41395) was used. The target cells were transduced with lentivirus containing pLIX-NEK2-WT and pLIX-NEK2-KD and selected with puromycin antibiotic 2μg/ml. For the expression of the transgenes, all the cell lines stably expressing inducible lenti vector were induced with 2-5 μg/ml of doxycycline (Sigma) for 24–96 h.

Culturing and maintenance of human iPSC culture

At least three different human iPSCs were used in this study, namely, mEGFP (AICS-0012), mRFP (AICS-0031) TUBA1B, and IMR90 (Wicell). Cells were plated on Matrigel (Corning) coated culture dishes for 1h at 37°C with 5% CO2 using mTeSR1 medium (STEMCELL technologies). Cultures were routinely tested for mycoplasma contamination using MycoAlert Kit (Lonza). Cells were dissociated into small aggregates using ReLeSR (STEMCELL technologies) every 5-7 days and split into freshly coated Matrigel culture dishes.

Astrocyte generation from NPCs

For the differentiation of astrocytes, a modified protocol was used for NPC generation (Shi et al., 2012). In brief, mycoplasma free iPSCs were seeded in matrigel-coated dishes. To start NPCs generation in 2D, iPSCs were grown until they reached 100% confluency. Optimized neural induction medium was used 1:1 mixture of DMEM/F12 (GIBCO) and Neurobasal (GIBCO), supplemented with 1:200 N2 supplement (GIBCO), 1:100 B27 supplement without vitamin A (GIBCO), 50μl 2-mercapthoethanol, 5μg/ml Insulin (Sigma), 1:100 L-Glutamin (GIBCO), and 1:100 MEM-NEAA (GIBCO), including two SMAD pathway inhibitors 2,5 μM dorsomorphin (Sigma) and, 10 μM SB431542 (Selleckchem) to drive differentiation of iPSCs to neural lineage.

The neural induction medium was changed every day, and cells were monitored for the morphological changes during the differentiation time between 8-10 days after plating. When the neuroepithelium sheet was properly formed, then cells were split in aggregates of 300 to 500 cells using Dispase 1mg/ml for 30-45 min at 37°C.

Aggregates were seeded into 6 cm coated PLO and Laminin plate with neural induction medium supplemented with 20ng/ml bFGF (Peprotech) and 10μM Rock inhibitor for 24h. bFGF is used to promote the expansion of NSCs but does not block neural differentiation. The medium was changed the next day with a neural maintenance medium. Low passages NPCs were used to start astrocyte differentiation. NPCs are splitted 24h before, and confluency was maintained to 100% when the medium is changed to astrocyte differentiation medium. Astrocyte differentiation medium contained Neurobasal (GIBCO) supplemented with 20ng/ml IGF1 (Peprotech), 10ng/ml Heregulin (Peprotech) 10ng/ml CNTF (Peprotech), 1x Glutamax (GIBCO), 1x B27 without vitamin A (GIBCO), 100μg/ml Primocin (InvivoGen).

The astrocyte differentiation medium was changed every day until the morphology change was observed. After 15 days, cells were split and analyzed for CD44, an intermediate astrocyte marker. The cells were maintained in the astrocyte differentiation medium until 80% of the cells expressed GFAP and S100β. Astrocyte growth medium,1:1 mixture of DMEM/F12(GIBCO) and Neurobasal (GIBCO), EGF 5ng/ml (Peprotech), B27 without vitamin A 1x (GIBCO), N2 (GIBCO), Primocin 100μg/ml (InvivoGen) was used to culture astrocytes.

Depletion of IFT88 by siRNA

Synthetic siRNA oligonucleotides were obtained from SMARTPool (Dharmacon). Naive U3047MG and Nek2-KD expressing U3047MG (1×10^6) were transfected with 40 nM siRNA targeting IFT88 or with a scrambled sequence (negative control siRNA) for 72h using TransIT-X2 Dynamic (Mirus) transfection kit. The expression of Nek2-KD was induced using doxycycline for another 48h after siRNA IFT88 transfection. The knockdown of IFT88 was assessed by immunofluorescence staining for IFT88. siRNA ON-Target plus - Control pool Non-targeting was used as a scramble siRNA.

Immunofluorescence microscopy and imaging of organoids

For live imaging, organoids were grown in 35 mm air diffusing low adherent plate Lumox dish (Sarstedt), which has low autofluorescence and high light transmission properties. Alternatively, we also used μ-Slide angiogenesis slides (Ibidi) for imaging live organoids. Images were acquired using a Leica SP8 laser scanning confocal microscope. Images were captured using 20X air objective. The resulting 8-bit image files were imported into Fiji (ImageJ 1.52i) and maximum intensity projected. Finally, the TIFF files from Fiji were processed using Photoshop (Adobe CC 2018).

Tissue cleared organoids were imaged using Zeiss LSM 880 Airyscan confocal microscope equipped with laser lines 405, 488, 561, and 633 nm, a GaAsP detector, two PMT detectors Plan-Neoflaur 10x/0.3, and Plan-Apochromat 20x/0.8 M27 objectives. The tissue organoids were placed in ECI in 35 mm air diffusing or μ-Slide angiogenesis slides while imaging. 3D image stacks were acquired for representative organoids. The interval between the stacks was kept 2-3 μm apart, depending on the size of the organoids. The captured image files were imported into Fiji. The data were further processed using Fiji, Adobe Photoshop CC 2018, and Adobe Illustrator CC 2018. The z stack videos were prepared using Fiji. Image-based quantifications were performed manually using Fiji.

Immunohistochemistry on patient-derived GSCs

GSCs were grown on coverslips fixed in 4% paraformaldehyde (PFA) or ice-cold methanol, for the PFA fixed cells permeabilization was performed with 0.5% Triton X-100 in PBS for 10 min, and then blocked with 0.5% fish gelatin in PBS for 1h at RT. Primary antibody labeling was performed for 1h at RT or overnight at 4°C, followed by three washes in PBS. Primary antibodies used in this study included mouse anti-γ-tubulin (Sigma-Aldrich), rabbit anti-Arl13b (Proteintech), mouse anti-acetylated tubulin (Sigma-Aldrich), rabbit anti-Nde1 (Proteintech), mouse anti-Nestin 4D11 (Novus Biologicals, Cambridge, USA), rabbit anti-Tuj1 (1:100, Sigma-Aldrich), mouse anti-Pax6 (DSHB, Iowa University, Iowa, USA), mouse anti-Nek2 (BD Bioscience), rabbit anti-OFD1 (Gift from Prof. Jeremy Reiter), mouse anti-AuroraA (Cell signaling), mouse anti-HDAC6 (Santa Cruz), mouse anti-CD133 (DSHB), mouse anti-CD15 (DSHB), mouse anti-PDGFR-a (Santa Cruz), rabbit anti-Sox2 (Millipore), mouse anti-FLAG (Sigma), rabbit anti- GFAP (Cell signaling), rabbit anti-N-cadherin (Abcam), rabbit anti-S100beta (Abcam), mouse anti-GT335 (Adipogen), rabbit anti-IFT88 (Proteintech). The following day, the cells were washed with PBS, incubated with fluorophore-conjugated secondary antibodies 1h at room temperature. Images were acquired using a Leica SP8 scanning confocal microscope and processed using Adobe Photoshop and Illustrator.

STED imaging was performed using TCS SP8 gSTED, Leica. Far-red depletion laser (STED-Laser 775nm) was used for STED imaging. The alignment between channels was monitored using the Gatta STED Nanoruler (Gatta quant, Germany) to monitor STED performance. The PL Apo 100x/1.40 Oil STED Orange (Leica) objective was used, resulting in 100 × overall magnification with ~50nm lateral and 120nm axial resolution. Signals were detected using gate able hybrid detectors (HyD). Nyquist sampling criteria were maintained during imaging to achieve X-Y resolution of 120nm. Images obtained were deconvoluted using Huygens essential deconvolution software. Line profiles were plotted based on fluorescent intensity values. The images were further processed using ImageJ and Adobe Photoshop.

GSCs invasion into brain organoid

Brain organoids were generated as previously demonstrated (Gabriel and Gopalakrishnan, 2017; Gabriel et al., 2017). In brief, mycoplasma-free iPSCs were cultured and checked for appropriate stem cell morphology. Once iPSCs reached 80% confluency cells were disassociated into single cells using Accutase (Sigma-Aldrich) for 5 min at 37°C. To start the organoid generation, 35.000 iPSCs were seeded into CellCarrier Spheroid ULA 96-well microplates (PerkinElmer) using neural induction medium (NIM, STEMCELL technologies) containing 10μM ROCK inhibitor Y-27632 (Biozol) for 24h. 100μl of the mix was suspended into cell suspension was given into each well of ULA 96 well U-bottom and incubated at 37°C in the presence of 5% CO2. This process helps in the formation of neurospheres, and the medium is changed once every day for the next 5days. At day-5, neurospheres were embedded a droplet of Matrigel (Corning) using organoid-embedding sheet (STEMCELL technologies). Droplets were solidified at 37°C and were grown four days without agitation in neurosphere medium containing a 1:1 mixture of DMEM/F12 and Neurobasal supplemented with N2 (1:200) (Thermo Fisher Scientific), B27 (1:100) supplement without vitamin A (Thermo Fisher Scientific), 50μl 2-mercapthoethanol, Insulin (Sigma), 1:100 L-Glutamin (GIBCO), and 1:100 MEM-NEAA (GIBCO). After four days, neurospheres were transferred to a spinner flask containing brain organoid medium which is essentially neurosphere medium supplemented with two SMAD pathway inhibitors 2,5 μM dorsomorphin (Sigma) and 25 μm SB431542 (Selleckchem).

To study GSCs invasion, 10-day old brain organoids were shifted to 35 mm air diffusing low adherent plate Lumox dish (Sarstedt) and 1000 GSCs were provided at the vicinity of the organoids as depicted in the experimental scheme (Figure 7). After 48h incubation, organoids with U3047MG Nek2-KD were induced with doxycycline. Organoids supplemented with GSCs before and after cilium induction were subjected to live imaging. The fixed organoids were supplemented with GSCs cells for 10-days, and then doxycycline was supplied for 10-days to induce expression of Nek2-KD. From this, organoids were selected for cryosection and tissue clearing followed by 3D imaging at day-20 after GSCs invasion.

Whole organoid tissue clearing

Tissue clearing was performed based on the previously described method adapting additional modifications and optimizations (Klingberg et al., 2017). In brief, organoids incubated with GSCs were fixed in 4%PFA (Merck Millipore) for 30 min. Organoids were dehydrated sequentially in graded ethanol (EtOH) series of 30% EtOH (vol/vol), 50% EtOH (vol/vol), 75% EtOH (vol/vol) and 100% EtOH (vol/vol) (each step for up to 5-10 min at 4°C in a gently shaking 2ml tube depending on the size of organoids). Subsequently, tissue clearing was performed with Ethyl cinnamate (ECI; Sigma Aldrich) for approximately 10-20 min at room temperature, depending on the size of organoids. Clarified organoids were then placed into coverslip bottom μ-slides (Ibidi) and stored at 4°C until imaging.

Fluorescence microscopy and immunofluorescence of brain tumor xenografts

Brains were frozen sectioned on the coronal plane (20 μm thick). For fluorescence microscopy, sections 120 μm apart were collected in distilled water and mounted on slides with Vectashield mounting medium (Bio-Optica, Milan, Italy). Images were acquired with a laser scanning confocal microscope (LSM 500 META, Zeiss, Milan, Italy). The cranio-caudal extension of the brain area invaded by fluorescent tumor cells was assessed on serial coronal sections.

For immunofluorescence, slices were rinsed three times at room temperature (10 min each) in PBS, and then blocked in PBS with 10% BSA, 0.3% Triton X-1000 for 2 hours. Sections were then incubated overnight at 4°C in PBS with 0.3% Triton X-1000, 0.1% normal donkey serum (NDS) with primary antibodies. For Arl13B detection, slices were incubated with the following primary antibodies: rabbit anti-Arl13B (1:200, Proteintech) or mouse anti-Arl13B (1:500, NeuroMab, Davis, CA, USA). Slices were then rinsed three times in PBS (10 min each) at room temperature and incubated in PB containing 0.3% Triton X-100 with secondary antibodies for 2 hours at RT. Secondary antibodies used were as follows: Alexa Fluor 647 or 555 donkey anti-mouse, and Alexa Fluor 555 or 647 donkey anti-rabbit secondary antibodies (1:500; Thermo Fisher Scientific, Waltham, MA).

Immunohistochemistry on human specimens

All patients provided written informed consent to the study according to research proposals approved by the Institutional Ethics Committee of Fondazione Policlinico Gemelli, UCSC (Prot. 4720/17).

Tissue samples were fixed in 4.5% formalin for 48 hours at 4°C, post-fixed in 30% sucrose, and sectioned (40 μm) by a cryostat. The sections were permeabilized overnight at 4°C in PBS with 0.3% Triton X-and 0.1% NDS with primary antibodies. Primary antibodies, rat anti-Collapsin Response-Mediated Protein 5 (CRMP5, 1:50, Millipore), mouse anti-γ-tubulin (1:50, Santa Cruz), rabbit anti-Arl13B (1:200, Proteintech). Following washed slices were incubated with fluorophore-conjugated secondary for 2h at room temperature. Images were acquired with a laser confocal microscope (Leica SP5).

Electron microscopy

GSCs were grown on coverslips and fixed with 2% glutaraldehyde (Electron Microscopy Sciences), and processed in electron microscopy as previously described (Gopalakrishnan et al., 2011, 2012). The embedded cell pellets were ultra-thin-sectioned (80 nm), counterstained, and visualized for ultra-structural details of centrosomes and cilia using a Zeiss 10A electron microscope. Images were processed using Adobe Photoshop.

Western blotting

Total protein from cultured cells was homogenized in RIPA lysis buffer with a mixture of protease and phosphatase inhibitors (Santa Cruz). Protein concentration was determined using the Bradford assay (Sigma-Aldrich), and samples were run on a 10% SDS-page gel. Primary antibodies used were mouse anti- CPAP (Hybridoma C44), mouse anti-Nek2 (BD Bioscience), rabbit anti-ODF2 (Proteintech), rabbit anti-GAPDH (Proteintech), rabbit anti-OFD1 (Gift from Prof. Jeremy Reiter), rabbit anti-Nde1 (Proteintech), mouse anti-AuroraA (Cell signaling), rabbit anti-Plk1 (Cell signaling), mouse anti-HDAC6 (Santa Cruz), mouse anti-GFP (Proteintech), rabbit anti-myc (Abcam), mouse anti-CD133 (DSHB), mouse anti-PDGFR-a (Santa Cruz), rabbit anti-AKT (Cell signaling), rabbit anti-phopho-AKT (Cell Signaling), rabbit anti-Sox2 (Millipore), mouse anti-FLAG (Sigma), rabbit anti-TUJ1 (Sigma), rabbit anti- GFAP (Cell signaling). Membranes were probed with horseradish peroxidase-linked donkey anti-rat IgG (1:5000), goat anti-mouse IgG (1:5000) and detection of protein was conducted using ECL western blotting reagents (Thermo Fisher). All western blots are representative images from at least three biological replicates.

FLAG-immunoprecipitation (IP) for CPAP and Nek2 complexes

Flag coated beads (Sigma Aldrich) were incubated with high-speed lysate (HSL) for 3h at 4°C. The lysates were prepared using HEK293T cells stable expressing pSIN CPAP-WT 3xflag and pLenti Nek2-WT 3xflag lysed with 1x BRB80 buffer (extract buffer) as described previously (Gopalakrishnan et al., 2011). After incubation, the beads were washed 3x times with extract buffer and washed 2x with high-salt buffer containing 500 mM salt, and final wash with buffer containing 100 mM NaCl, the samples were eluted by boiling them in 2x Laemmli buffer at 98°C. The beads were analyzed by western blotting for the CPAP and Nek2-complexes.

RNA sequencing and analysis

U3047MG (before ciliation) and U3047-Nek2-KD (after ciliation) cells were collected and washed once with cold PBS before adding to 300 μl Tri-Reagent (Sigma Aldrich, USA) by free-thawing, and total RNA was isolated and DNase-treated using the DirectZol RNA kit (Zymo Research). Approximately 2 μg of total RNA was used to subselect poly(A)$^+$ transcripts and generate strand-specific cDNA libraries (TrueSeq kit; Illumina).

Poly(A)-enriched RNA was prepared and sequenced on a HiSeq4000 platform (Illumina; strand-specific) to > 35x106 reads per sample. Reads were quality assessed and mapped to hg19 using STAR (Dobin et al., 2013), followed by quantification of unique exon counts using featureCounts (Liao et al., 2014). Counts were further normalized via the RUVs function of RUVseq (Risso et al., 2014) to estimate factors of unwanted variation using those genes in the replicates for which the covariates of interest remain constant and correct for unwanted variation, before differential gene expression was estimated using DESeq2 (Love et al., 2014). Genes with an FDR < 0.01 and an absolute (log2) fold-change of > 0.6 were deemed differentially-expressed and listed in Table S1.

To cross check the existing datasets, first, we retrieved the gene read count matrix (accession number GSE61586) and analyzed for differential expression using a BioJupies Python Notebook (https://pubmed.ncbi.nlm.nih.gov/30447998/; https://pubmed.ncbi.nlm.nih.gov/23603901/) using a level of significance of 0.05 for the adjusted p value. The heatmap was generated from the count matrix in R, using the heatmap R package.

QUANTIFICATIONS AND STATISTICAL ANALYSIS

Data were analyses statistically using GraphPad Prism 7 for Mac OS X (Version 7.0e, September 5, $f$way ANOVA, followed by Sidak's multiple comparisons test or Tukey's multiple comparisons test or unpaired t test or Dunnett's multiple comparisons test. n.s, indicates no significance, *$p < 0.05$, **$p < 0.01$, ***$p < 0.001$.